

Wavepacket and Reduced-Density Approaches for High-Dimensional Quantum Dynamics: Application to the Nonlinear Spectroscopy of Asymmetrical Light-Harvesting Building Blocks

Joachim Galiana,^{†,¶} Michèle Desouter-Lecomte,[‡] and Benjamin Lasorne^{*,†}

[†]*ICGM, Univ Montpellier, CNRS, ENSCM, Montpellier, France*

[‡]*Institut de Chimie Physique, Université Paris-Saclay-CNRS, UMR8000, F-91400 Orsay, France*

[¶]*Current affiliation: Departamento de Química, Universidad Autónoma de Madrid, Madrid, Spain*

E-mail: benjamin.lasorne@umontpellier.fr

Abstract

Excitation-energy transfer (EET) and relaxation in an optically excited building block of poly(phenylene ethynylene) (PPE) dendrimers are simulated using wavepackets with the multilayer multiconfiguration time-dependent Hartree (ML-MCTDH) method and reduced-density matrices with the hierarchical equations of motion (HEOM) approach. The dynamics of the ultrafast electronic funneling between the first two excited electronic states in the asymmetrically *meta*-substituted PPE oligomer with two rings on one branch and three rings on the other side, with a shared ring in between, is treated with 93-dimensional *ab initio* vibronic-coupling Hamiltonian (VCH) models, either linear or with bilinear and quadratic terms. The linear VCH model is also used to model an open quantum system. The linear-response absorption and emission spectra are simulated with both the ML-MCTDH and HEOM methods. The latter is further used to explore the nonlinear response regime and the expected EET fingerprint in the time-resolved transient absorption (TA) spectra and excited stimulated emission (ESE) with delta-like impulsive laser pulses.

Keywords: high-dimensional quantum dynamics, open quantum dynamics, excitation-energy transfer, nonlinear spectroscopy, light-harvesting dendrimers.

1 Introduction

The photophysics and ultrafast funneling dynamics in tree-like poly(phenylene ethynylene) (PPE) dendrimers have drawn a great interest since their original synthesis in 1995.¹ They have been extensively studied, both experimentally^{2–6} and theoretically,^{7,8} for their astonishing light-harvesting properties. In the present work, we investigate such features in an asymmetrical building block, for which we extract time-dependent spectral fingerprints of ultrafast electronic excitation-energy transfer (EET) from simulations with performant quantum-dynamics methods using an *ab initio* calibrated vibronic coupling Hamiltonian (VCH) model in full dimensionality as regards in-plane motions (93 vibrational modes).

Simulating energy-resolved molecular photodissociation or light-absorption cross-section spectra from time-dependent wavepacket quantum dynamics has been triggered by the seminal work of Heller in the late 1970s.⁹ Rather than diagonalising a molecular Hamiltonian – which becomes rapidly impracticable for high-dimensional molecular systems – it was then proposed that propagating a wavepacket and taking the Fourier transform of its auto-correlation function – so as to get a power spectrum – could be a less-expensive avenue from a numerical point of view.

Such a realisation may be considered as a milestone in the

history of wavepacket quantum dynamics within the ‘molecular physics and theoretical chemistry’ communities, which perhaps found its acme with the release of the multiconfiguration time-dependent Hartree (MCTDH) method^{10,11} – able to treat molecules with about tens of atoms – and its landmark applications in the late 1990s and early 2000s to the calculations of the photoexcitation spectrum of pyrazine and the photoionisation spectrum of butatriene,^{12,13} in perfect agreement with experiments. Extensions to higher-dimensional systems, such as the multilayer version of MCTDH (ML-MCTDH) have been designed since then so as to handle molecules with about hundreds of atoms.^{14–16}

The spectral method proposed by Heller is a linear-response approach based on first-order time-dependent perturbation theory. It is justified, *via* Fourier-transform relations between time/energy-resolved Green’s functions (propagator/resolvent), from the equivalence of the sudden dynamical response of a system to a spectrally “white” Dirac delta pulse in time (flat-intensity, phaseless, and infinitely broad spectrum) with the sequence of light-matter resonances induced by tunable continuous waves that monitor at each transition energy the spectral density of states of the unperturbed Hamiltonian so as to produce a cross section.

While such an approach was originally designed for providing the weak-field limit (one photon) of the absorption/excitation spectrum to be recorded in steady-state spec-

troscopy, it quickly became a computational way for mimicking the time-resolved effect of a very short pulse (sudden or impulsive Condon approximation) due to the emergence of pump-probe femtochemistry,¹⁷ designed to monitor – and ultimately control – the ultrafast photochemical/photophysical response of molecules to the excitation by UV-visible light pulses.

This triggered a vast literature within computational photochemistry, often related to applications of the hybrid quantum-classical trajectory surface hopping (TSH) method.^{18,19} Typically, such calculations – aimed at the description of low-temperature and almost isolated molecules – assume a vibrational Wigner distribution in the electronic ground state and a sudden projection of the nuclear wavepacket distribution – viewed as a statistical ensemble of initial conditions in phase space – to the excited electronic state to be probed. Various alternative approaches followed in the field of nonadiabatic molecular dynamics.^{20–22}

Interestingly enough, linear-response and/or real-time time-dependent density functional theory (LR/RT-TD-DFT)^{23,24} emerged over the same era, based on similar theoretical foundations (first-order time-dependent perturbation theory), as a practicable quantum-chemistry method aimed at addressing the excited electronic states of large molecules, less expensive than wavefunction-based approach, but subject to some limitations (charge-transfer states are poorly described; doubly-excited contributions are absent; conical intersections between the ground state and the first singlet excited state are not described correctly). Yet, this allowed the development of approaches capable of producing vibronically-resolved absorption and emission spectra, beyond the vertical-transition approximation, but under the Born-Oppenheimer approximation.^{25–27}

More recently, some pressing questions have arisen within the theoretical/computational community about what we actually simulate and how we should better relate to time-resolved spectroscopy experiments beyond linear response. Indeed, since Mukamel’s seminal works^{28,29} there has been a clear incentive for theoretical chemistry to address nonlinear and/or two-dimensional spectroscopy techniques, which are no longer exotic but rather the new standard.^{30–34}

In addition, taking into account the role of the environment that surrounds the molecule (dissipation, solvent and thermal effects, *etc.*) with an adequate formalism (density operators rather than wavepackets and the Liouville master equation rather than the Schrödinger time-evolution equation) has become crucial again in this context. This has led to many flavours of open quantum dynamics approaches, one of them – used in the present work – being known as the hierarchical equations of motion (HEOM) method,^{35–40} in which vibrations are considered as a continuous bath (with a statistical spectral density) coupled to the discrete electronic subsystem (quantum few-level reduced-density matrix).

Within the field of time-resolved spectroscopy, what is customarily known as transient absorption (TA) is defined as the differential absorbance within a pump-probe context: namely, $\Delta A = A(w/\text{pump}) - A(w/o\text{ pump})$ (aka. differential optical density). Hereby, we investigate a nonlinear time(delay)-and- (transition)energy-dependent light-

emission signal, known as dispersed and integrated TA in the limiting case of impulsive laser pulses. The TA polarization can be estimated from the three-pulse photon-echo 2D polarization upon assuming that the first two pulses overlap.^{29,41} The third-order polarization is due to two interactions of the pump pulses and one of the probe pulse. TA bears some resemblance with the so-called transient grating (TG) signal because the third-order polarization in TA is identical to that in TG, only the measurements are different in TA and TG.⁴²

The TA signal results from two positive contributions to the optical coherence: the excited-state stimulated emission (ESE) [the emitting species is emitting more upon production] and the ground-state bleaching (GSB) [the absorbing species is absorbing less upon depletion]. An additional emission-quenching process, the excited-state absorption (ESA), manifests itself as a negative contribution to this signal.

In the present work, ESA is not considered, but we assume a two-excited-state vibronically coupled manifold that can be excited and can emit within two distinct spectral ranges and undergo mutual internal conversion in the form of EET. Our simulations show that the early TA signal is dominated by pure GSB first (what is emitting is due to what has just been absorbing from the equilibrium ground state: reciprocal absorption) until reaching an asymptotic regime with a stabilization to pure ESE (what is emitting is due to what has finally relaxed in the excited-state manifold). While such early and late behaviors are expected, the detailed kinetics at intermediate time delays is not evident due to EET, and we examine how its fingerprint can be detected in some post-processed signals.

Our system of interest for simulating such signals is the exhaustively studied asymmetrically *meta*-substituted PPE oligomer, made of four phenyl or phenylene rings and three acetylenic bonds, called m23 in the following (fig. 1 a). This building block of PPE dendrimers was shown to be an ideal model system for EET, having two distinct localized excitons as its first two singlet electronic excited states (see fig. 1, b and c).^{43–45}

Full-dimensional simulations of the photoinduced dynamics of m23 were originally exposed by Fernandez-Alberti and co-workers using the aforementioned TSH method^{43,46} and the multiconfiguration Ehrenfest approach.⁴⁷ Such simulations were also recently used to produce nonlinear spectroscopic signals to study exploitable spectral signatures of EET.⁴⁸ This is also one of the aims of the present work.

We recently proposed a quantum wavepacket study (based on MCTDH) of the photoinduced dynamics of m23 with dimensionally reduced VCH models obtained from its *ab initio* potential energy surfaces (PESs).⁴⁵ Such a strategy was concomitantly followed by other authors to go toward higher-dimensional model, using a wavepacket tensor-train formalism.⁴⁹ Here, we revisit the photodynamics of m23 with both the ML-MCTDH wavepacket and HEOM reduced-density approaches, using a systematic parametrization procedure for generating VCH models adapted to two-exciton systems in high dimensionality.

The paper is organized as follows. In the second section, we describe our procedure for the realistic parametrization

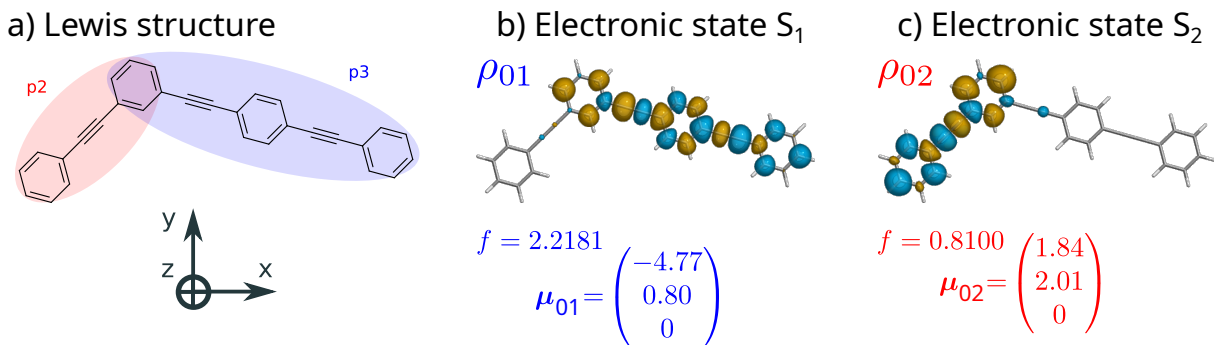


Figure 1: a) Lewis structure associated to the Franck-Condon geometry of the first asymmetrical *meta*-substituted PPE oligomer, called m23 in the following. The Cartesian axes are also given. b) and c) Transition density, oscillator strength, and transition dipole moment (in atomic units) for each of the first two singlet electronic excited states at the Franck-Condon geometry.

of both the discrete and continuous high-dimensional models that are used for ML-MCTDH and HEOM dynamics, respectively, and recall the underlying formalism for calculating various spectroscopic responses from simulations. In the third section, we first provide and compare time-resolved electronic populations and steady-state spectra obtained with both approaches within linear response. We continue with an exposition of nonlinear transient signals and discuss how they may provide a fingerprint for EET. Concluding remarks and outlook are gathered in the last section.

2 Methods and Concepts

2.1 The models and their Hamiltonians

2.1.1 High-dimensional vibronic coupling Hamiltonians

Within an *ab initio* adiabatic description, the electronic system of the m23 molecule is reduced herein to its electronic ground state, S_0 , and its first two bright singlet electronic excited states, S_1 and S_2 , which are nonadiabatically coupled and have been described in detail in previous works.^{43–45}

The minima of the S_0 (Franck-Condon point; FCP), S_1 , and S_2 states, and their frequencies, as well as the minimum-energy conical intersection (MECI) between S_1 and S_2 , and its branching-space vectors, have all been optimized and characterized previously with DFT and TD-DFT calculations (CAM-B3LYP/6-31+G* level of theory)⁴⁵ using the GAUSSIAN 16 (Revision A.03) quantum-chemistry software package.⁵⁰ In particular, it has been shown that S_1 is locally excited on the 3-ring branch p3 (at 3.88 eV) while S_2 is locally excited on the shorter 2-ring branch p2 (at 4.55 eV). The corresponding transition densities are given in fig. 1, b) and c), together with the electronic transition dipole moments and oscillator strengths.

In order to run our simulations, we have parametrized a diabatic high-dimensional VCH model for the ground state S_0 and the two coupled PESs of the singlet electronic excited states S_1 and S_2 of m23 with all the $N = 93$ in-plane (A') normal modes of vibration. Such a type of model refers to as a ‘diabatization by Ansatz’. At the FCP, the two excited

diabatic states that form the interacting basis set, D_1 and D_2 , coincide with the adiabatic ones, S_1 and S_2 by construction. All the in-plane modes are involved *a priori* in both the intra-state energy and inter-state coupling gradients for the first two electronic excited states (of same symmetry A'). Such a selection includes in particular the dominant quinoidal and acetylenic modes, previously identified as being essential for EET in the PPE dendrimers,^{43,45,51–53} here augmented with extra low-frequency modes and C–H vibrations.

Our most sophisticated model Hamiltonian is in-between the customary linear vibronic coupling (LVC) and the full quadratic vibronic coupling (QVC) models; namely, the off-diagonal bi-linear terms are set to zero here, but diagonal quadratic and bi-linear terms remain flexible (three approximate flavors of it will be discussed in what follows). The model Hamiltonian matrix (centered at the FCP geometry) thus reads

$$\mathbf{H}(\mathbf{Q}) = \begin{pmatrix} 0 & 0 & 0 \\ 0 & E^{(1)} & 0 \\ 0 & 0 & E^{(2)} \end{pmatrix} + \left(\widehat{T}_{\text{nu}} + \sum_i \frac{1}{2} k_i^{(0)} Q_i^2 \right) \mathbb{1}_3 + \sum_i \begin{pmatrix} 0 & 0 & 0 \\ 0 & \kappa_i^{(1)} Q_i & 0 \\ 0 & 0 & \kappa_i^{(2)} Q_i \end{pmatrix} + \sum_i \begin{pmatrix} 0 & 0 & 0 \\ 0 & 0 & h'_i Q_i \\ 0 & h'_i Q_i & 0 \end{pmatrix} + \sum_i \sum_j \begin{pmatrix} 0 & 0 & 0 \\ 0 & \frac{1}{2} \gamma_{ij}^{(1)} Q_i Q_j & 0 \\ 0 & 0 & \frac{1}{2} \gamma_{ij}^{(2)} Q_i Q_j \end{pmatrix}, \quad (1)$$

where \widehat{T}_{nu} is a typical one-state normal-mode nuclear kinetic-energy operator and the second matrix (proportional to the identity matrix) is the harmonic reference, parametrized at the minimum of the electronic ground state (FCP) through the knowledge of the frequencies $\omega_i^{(0)2} = k_i^{(0)}$ (assuming mass-weighted normal coordinates, Q_i).

The curvatures of the electronic excited states are allowed to be different together and with the electronic ground state (thus including Duschinsky effects) thanks to the diagonal quadratic terms $\gamma_{ii}^{(s)}$. In other words, we model the PESs with a Taylor expansion to the second order for the diabatic potential energies (diagonal) and to the first order for the inter-

state coupling (off-diagonal).

In the following, we shall refer to eq. (1) as the LVC+ γ model. From it, we define the pure LVC model, upon setting the last matrix to zero (quadratic corrections and bi-linear mode mixings). The intermediate model with quadratic corrections obtained from the LVC+ γ model but restricted to $i = j$ for γ_{ij} will be called LVC+ γ_{ii} .

The LVC model will be used as the system-bath Hamiltonian associated to our open quantum system (see below). Within second quantization, it may be termed a Frenkel-Holstein excitonic Hamiltonian (in relation with the p2 and p3 locally excited states) coupled to a harmonic bosonic bath, or a spin-boson model as regards the two-level excited manifold at the FCP (D_1 and D_2).

Local fitting procedure *via* identification of energy derivatives

Herein, we give details about the parametrization of the model Hamiltonian defined in eq. (1). It uses: i) the vertical transition energies, gradients, and Hessians at the FCP; ii) the position (with respect to FCP) of the MECI, $\Delta\mathbf{Q}_X$, and the branching-space vectors, (\mathbf{g}, \mathbf{h}) , at this geometry.

The strategy for ensuring that the diabatic and adiabatic states coincide at both the FCP and MECI geometries is similar to the one used in a previous study on a dimensionally-reduced model for m23.^{45,54} The orthogonal pair of branching-space vectors, (\mathbf{g}, \mathbf{h}) , is obtained numerically from the Hessian of the squared energy difference at the MECI, and is rotated into a pair of new branching-space vectors, $(\mathbf{g}', \mathbf{h}')$, such that

$$\mathbf{h}' \cdot \Delta\mathbf{Q}_X = 0 \quad , \quad (2)$$

where the \mathbf{h}' -vector components define the off-diagonal parameters in eq. (1). With the 93 selected normal modes, the parametrized rotation angle is $\theta = 18.82^\circ$, which accounts for a moderate photochemical reaction-path curvature (second-order relaxation) from FCP to MECI.

We now focus on the parameters for the diabatic potential energies. The diabatic energies at the FCP geometry, $E^{(s)}(\mathbf{Q} = \mathbf{0})$, simply identify to the adiabatic vertical transition energies of S_1 and S_2 . Similarly, the diabatic gradients can be made identical to the adiabatic gradients of S_1 and S_2 within a Hellmann-Feynman spirit for a local crude-adiabatic representation.

The generation of the curvatures and bi-linear cross-terms for the excited diabatic states is more involved. The matrices $\gamma^{(s)}$ (which account for intra-state mode mixing) cannot be directly identified to the vertical transition Hessians of the adiabatic states S_1 and S_2 . Indeed, because we defined an inter-state coupling gradient, \mathbf{h}' , the definition of the diabatic Hessians (sums of the ground-state Hessian \mathbf{K}_{S_0} and the $\gamma^{(s)}$ matrices) must reflect the effect of the coupling when producing the adiabatic Hessians. To ensure this, we define the diabatic Hessians as, according to a second-order Jahn-

Teller-type formula,⁵⁵

$$\begin{aligned} \mathbf{K}_{S_0} + \gamma^{(1)} &= \mathbf{K}_{D_1} = \mathbf{K}_{S_1} + 2 \frac{\mathbf{h}'\mathbf{h}'^T}{E_{S_2} - E_{S_1}} \quad , \\ \mathbf{K}_{S_0} + \gamma^{(2)} &= \mathbf{K}_{D_2} = \mathbf{K}_{S_2} - 2 \frac{\mathbf{h}'\mathbf{h}'^T}{E_{S_2} - E_{S_1}} \quad . \end{aligned} \quad (3)$$

Such an effect is physically motivated but occurs here to have little consequences numerically, only because the FCP energy gap, $E_{S_2} - E_{S_1}$, is large enough (a more detailed analysis is provided in SI, section SI-I and fig. SI-1).

Let us recall that we have restricted ourselves to the 93 in-plane normal modes of the m23 molecule herein. Overall, the most important values of the Hessians occur to be on-diagonal. In other words, the normal modes of S_0 almost form an orthonormal eigenbasis for the Hessians of the excited states (almost diagonal matrices). This means that there is little mode mixing, as proven by the small magnitude of the elements of the matrices $\gamma^{(s)}$. They are also shown in SI, fig. SI-1. Such an analysis can be related to the evaluation of Duschinsky matrices, only with the fact that, here, the excited states are computed at the same geometry as the ground-state equilibrium geometry.

However, let us examine, for the mode-mixing matrices, $\gamma^{(s)}$, some finer features as regards the frequencies of the normal modes. There are greater values (hence greater mode mixing) for the group of quinoidal and acetylenic modes (from 1600 cm^{-1} to 2400 cm^{-1}), both among them and with the other modes. To some extent, this is also true for the triangular modes (from 1000 cm^{-1} to 1600 cm^{-1}), with significant mode-mixing among them (see SI, fig. SI-1).

The previous analysis can serve two different (but not unrelated) purposes: i) finding mode-combination strategies for optimally taking into account the correlation between the strongly mixing modes; ii) establishing relevant system-bath partitions wrt. active modes (as regards spectroscopy and EET) and spectator modes. Such considerations are expected to help in forming a rationale for designing an optimal tree for ML-MCTDH simulations under high-rank-tensor compression approaches.

Validity and limitations of the local fitting procedure

The electronic energies at the minimum of S_0 (FCP) are set with no ambiguity from the onset. Now, in order to evaluate the validity of our VCH approximate descriptions, we should compare the energies of the *ab initio* S_1 and S_2 adiabatic states at some critical points (obtained with routine optimization procedures) to the model eigenvalues. The electronic energies at the minima of S_1 , S_2 , and at the MECI are given in table 1.

First, we can remark the excellent energy agreement as regards the S_1 minimum (Min S_1) obtained within our 93-dimensional LVC + γ model and the true S_1 minimum of the *ab initio* PESs. However, the S_2 minimum (Min S_2) obtained within our 93-dimensional LVC + γ model occurs to merge numerically with an S_1/S_2 conical intersection, which is a perfectly acceptable situation when the MECI is peaked (the S_2 minimum is the MECI). Since the *ab initio* S_2 min-

Table 1: Energies in eV of the first two adiabatic and diabatic excited states at the critical points in the *ab initio* PESs (at the CAM-B3LYP/6-31+G* level of theory) and in the LVC model (8-dimensional, from previous work⁴⁵), and LVC+ γ model (present work; 93-dimensional).

Model Critical Point	Full-dimensional (<i>ab initio</i>) ^a			8-dimensional (LVC)			93-dimensional (LVC + γ)		
	MinS ₁	MinS ₂	MECI	MinS ₁	MinS ₂	MECI	MinS ₁	MinS ₂	MECI ^b
$E(S_1)$	3.61	3.99	4.30	3.67	4.00	4.40	3.62	4.13	–
$E(S_2)$	4.62	4.17	4.30	4.59	4.23	4.40	4.64	4.13	–
$\Delta E(S_1 - S_2)$	1.01	0.18	$< 5e^{-4}$	1.08	0.23	$< 5e^{-3}$	1.02	$< 5e^{-3}$	–
$E(D_1)$	–	–	–	3.67	4.01	4.40	3.64	4.13	–
$E(D_2)$	–	–	–	4.59	4.22	4.40	4.62	4.13	–

^aDiabatic energies are not determined directly from *ab initio* calculations but are post-processed for the VCH models.

^bFor the 93-dimensional VCH model, the effective MECI occurs to be peaked and thus merges with MinS₂.

imum (MinS₂) exists, the *ab initio* MECI should in fact be slopped (at least slightly). Such small discrepancies are to be expected from a model that is imperfect as regards anharmonicity effects. Yet, we expect that the semi-quantitative orders of magnitude shown here are good enough for our model to be relevant.

2.1.2 Parametrization as an open quantum system

An open quantum system results from the bipartite partition of a complex system into an active sub-system treated by quantum mechanics coupled to an environment described by collective bath modes and statistical mechanics.^{56–58} The corresponding generic Hamiltonian matrix of the full system is split into three contributions,

$$\mathbf{H} = \mathbf{H}_S + \mathbf{H}_{SB} + \mathbf{H}_B, \quad (4)$$

where \mathbf{H}_S is the Hamiltonian of the open biexcitonic (three-level) system, associated here to the partition of the electronic degrees of freedom from all the vibrational (bosonic) modes. It is represented by the first diagonal matrix of eq. (1), with the energies at the FCP geometry of the ground state (set to zero) and of the two excited states, $E^{(1)}$ and $E^{(2)}$.

The environment is a collection of $N = 93$ harmonic vibrational modes centered at the origin (FCP point) and associated to the ground-state frequencies. It is represented by \mathbf{H}_B and given by the second matrix of eq. (1).

Such bosonic modes are separated into N_{bath} baths that make the effective electronic energies and inter-state coupling fluctuate to first order wrt. the \mathbf{H}_S reference. The system-bath coupling is given by the third and fourth matrices of the LVC model in eq. (1). It can be recast as $\mathbf{H}_{SB} = \sum_n^{N_{\text{bath}}} \mathbf{S}_n B_n$, where \mathbf{S}_n are the matrices of the projection and transition operators wrt. the electronic states of the system. The corresponding excitonic Pauli-type system operators are $\hat{S}_1 = |1\rangle\langle 1|$, $\hat{S}_2 = |2\rangle\langle 2|$, and $\hat{S}_3 = |1\rangle\langle 2| + |2\rangle\langle 1|$, respectively.

The collective modes, B_n , are bosonic-type operators given here in coordinate representation for notational simplicity. Note that they do not appear as such in the HEOM equations but only *via* their statistical correlation functions, as described below. Three collective modes B_n are used here ($N_{\text{bath}} = 3$). The first two, $B_1 = \sum_j \kappa_j^{(1)} Q_j$ and $B_2 =$

$\sum_j \kappa_j^{(2)} Q_j$, are defined from the gradients of the PESs at the reference FCP geometry. They are called tuning collective modes since they make the electronic energy gap vary to first order. The third collective mode, $B_3 = \sum_j h_j Q_j$, is the coupling mode, which induces a first-order electronic inter-state coupling.

The B_n magnitudes have the dimension of an energy. We can define three associated mass-weighted collective coordinates of the baths from the 93 mass-weighted normal coordinates – upon normalization with the lengths of the mass-weighted gradient vectors – as $X_n = B_n/D^{(n)} = \sum_j^N f_j^{(n)} Q_j/D^{(n)}$, with $D^{(n)} = \sqrt{\sum_j^N f_j^{(n)2}}$ and $f_j^{(n)} = \kappa_j^{(n)}$ for the tuning baths, $n = 1, 2$, and $f_j^{(3)} = h_j$ for the coupling bath. Note that, within the harmonic model, the gradients and frequencies of each mode are directly related to the positions of the minima of the excited diabatic PESs of the LVC model wrt. the FCP point, $Q_{j0}^{(n)}$, *via* $\kappa_j^{(n)} = \omega_j^2 Q_{j0}^{(n)}$ (with $n = 1, 2$).

The evolution of the system reduced-density matrix, $\rho_S(t) = \text{tr}_B[\rho(t)]$, obtained upon tracing out the bath degrees of freedom, is given by a non-Markovian master equation. When the bath is harmonic, it follows Gaussian statistics and the main tool of the master equation is the matrix of the two-time correlation functions of the bath collective modes, $C_{mn}(t) = \langle B_n(t) B_m(0) \rangle_{\text{eq}}$, where $B_n(t)$ is the time-evolved Heisenberg representation of the operator and $\langle \bullet \rangle_{\text{eq}}$ denotes the average over a Boltzmann distribution at some given temperature T .

We neglect here any correlation among the modes of the three baths and consider only diagonal terms $C_{nn}(t) = \langle B_n(t) B_n(0) \rangle_{\text{eq}}$, with $n = 1, 2, 3$, which will further be denoted $C_n(t)$ with a single index for the sake of simplicity. The correlation functions may be computed with molecular dynamics in order to have an exhaustive description of the solvent.^{59–61} In this work, it is obtained *via* the spectral densities that encode the interaction of the baths at each frequency.

In a first step, discrete spectral densities involving the LVC Hamiltonian parameters only are given by

$$J_n(\omega) = \frac{\pi}{2} \sum_k \frac{f_k^{(n)2}}{\omega_j} \delta(\omega - \omega_j) \quad . \quad (5)$$

They peak at all individual vibrational frequencies, ω_j , and form a Dirac comb. In order to account qualitatively for the existence of some dissipative environment and decaying mechanisms, the Dirac delta distributions are broadened by a single spectral width, Γ , so as to be approximated as Lorentzian functions,

$$\delta(\omega - \omega_j) \sim \frac{1}{\pi} \frac{\Gamma}{(\omega - \omega_j)^2 + \Gamma^2}, \quad (6)$$

thus leading to a continuous spectral density. This is a typical smoothing approach that has been used in another context (MCTDH dynamics) in order to systematically reduce the number of active modes.^{62,63} In the absence of any further information on the dissipative environment, we adopted this heuristic procedure and we took $\Gamma = 160 \text{ cm}^{-1}$, giving a spectral line enlargement of the same order of magnitude as in a previous simulation on the m22 dimer.⁵³ Interestingly enough, such a procedure conserves the so-called reorganization energy, again involving the LVC Hamiltonian parameters only,

$$\lambda^{(n)} = \frac{1}{2} \sum_{j=1} \frac{\kappa_j^{(n)2}}{\omega_j^2}. \quad (7)$$

This may be important when the goal is a selection of a sample of new discrete modes that are possibly unitarily transformed to a hierarchical chain of coupled neighboring modes.⁶²⁻⁶⁴ The corresponding spectral densities are shown in fig. 2.

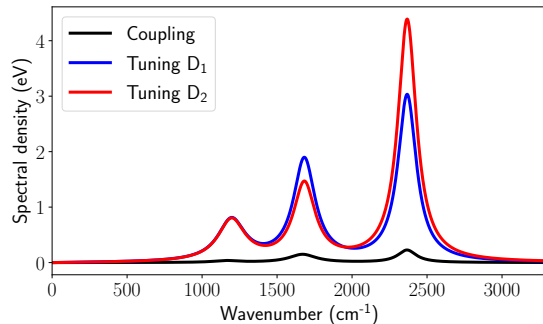


Figure 2: Spectral densities associated to the correlation functions for the three baths (tuning for D_1 , tuning for D_2 , and inter-state coupling between them.)

Within this context, the correlation functions are given by the following Fourier transforms,

$$C_n(t-t') = \frac{\hbar}{\pi} \int_{-\infty}^{\infty} d\omega J_n(\omega) \tilde{n}_\beta(\omega) e^{-i\omega(t-t')} \quad , \quad (8)$$

where $\tilde{n}_\beta(\omega) = (1 + \coth(\beta\hbar\omega/2))/2$ is the temperature-dependent Bose function with $\beta = 1/k_B T$, and k_B is the Boltzmann constant. We take here the standard room temperature, $T = 298 \text{ K}$.

Note that, being the reciprocal Fourier transforms of the two-time correlation functions $C_n(t-t')$ (of the B_n linear energy variations), the products $J_n(\omega)\tilde{n}_\beta(\omega)$ are sometimes called temperature-dependent power spectral densities (per frequency unit) and thus have the dimension of an energy.

$J_n(\omega)$ can be viewed as their zero-temperature limits, since the Bose distribution tends to one. Also, let us stress out here that the symbol ω , as used in our various equations, duly refers to an actual angular frequency (an angle variation per unit of time). However, for the sake of ease of comparison, we customarily provides its values in terms of its equivalent wavenumber (given in reciprocal centimeters), such is in fig. 2.

2.2 Propagated quantities and time-evolution equations

2.2.1 Quantum wavepacket propagation

Using the aforementioned VCH models, quantum dynamics calculations were carried out using the ML-MCTDH method, as first implemented in the Heidelberg MCTDH package and further integrated to the QUANTICS suite of quantum-dynamics programs.^{10,11,65}

The primitive basis set was defined with 15 harmonic-oscillator (Gauss-Hermite) basis functions per mode, with the equilibrium geometry set to zero (the FCP origin), effective masses set to one (reduced masses included in the mass-weighted coordinates), and ground-state frequencies for each normal mode of the model.

The multilayer tree was built according to a strategy meant to reflect the different types of molecular vibrations among the 93 normal modes. Four groups are defining the upper layer: low- and high-frequency modes with small reduced masses (frequencies: 0 cm^{-1} to 1000 cm^{-1} and 2400 cm^{-1} to 3500 cm^{-1} , for soft modes and rigid C-H elongations, respectively), and two sets of high-frequency modes with large reduced masses (frequencies: 1000 cm^{-1} to 1500 cm^{-1} and 1500 cm^{-1} to 2400 cm^{-1} , which gather triangular, quinoidal, and acetylenic modes). The latter group reflects the three-peak features of the spectral density shown in fig. 2.

The rest of the tree was simply built from this first layer (four nodes) down to a third layer where the individual modes are combined two by two. The number of single-particle functions (SPFs) for each node and combined modes was chosen so as to maintain a reasonable computational time ($< 24 \text{ h}$ of human time on a 16-core CPU for 200 fs) and small lowest natural weights ($< 1 \times 10^{-2}$) throughout the simulation. A detailed representation of the ML-tree is given in SI, fig. SI-3.

2.2.2 Hierarchical equations of motion

The HEOM method^{35-39,66} for simulating the dissipative dynamics of an open quantum system relies on solving a non-Markovian master equation. It is exact for harmonic baths characterized by Gaussian statistics when the hierarchy is truncated soundly. The central point of the HEOM formalism is the expansion of the correlation functions for each bath, $C_n(t)$, and of their complex conjugates, $\bar{C}_n(t)$, as sums of ordered contributions.

The most popular expression, adopted here, is a weighted

sum of K_n rotating and decaying exponential functions,

$$C_n(t) = \sum_{k=1}^{K_n} \alpha_k^{(n)} e^{i\gamma_k^{(n)} t} \quad , \quad (9)$$

with complex amplitudes and phases, α_k and $\gamma_k = \Omega_k + i\Gamma_k$, for each bath. Every term corresponds to a so-called ‘‘bath artificial decay mode’’, with positive decay rate, Γ_k , and positive or negative rotating frequency, Ω_k , associated to the absorption or emission energy between the system and the bath.

The HEOM formalism consists in a local-in-time system of coupled equations among auxiliary matrices, also called auxiliary density operators (ADOs). Each ADO has the dimension of the system reduced-density matrix, here 3×3 , and is labelled by a global index-vector denoted $\mathbf{m} = (m_1, \dots, m_k, \dots, m_K)$, which gives the occupation number of each artificial mode. The system reduced-density matrix is $\rho_S = \rho_{\mathbf{m}=\mathbf{0}} = \rho_{0, \dots, 0}$, with all the m_j indices in \mathbf{m} set to zero. The number $K = \sum_n^{N_{\text{bath}}} K_n$ represents the total number of artificial modes belonging to the N_{bath} baths (size of the \mathbf{m} -vector).

The hierarchical master equations for the ADOs thus take the following form,

$$\begin{aligned} \dot{\rho}_{\mathbf{m}}(t) = & \mathbf{L}_S \rho_{\mathbf{m}}(t) + i \sum_n^{N_{\text{bath}}} \sum_{k=1}^{K_n} m_k^{(n)} \gamma_k^{(n)} \rho_{\mathbf{m}}(t) \\ & - i \sum_n^{N_{\text{bath}}} \left[\mathbf{S}_n, \sum_{k=1}^{K_n} \rho_{\mathbf{m}_k^{+(n)}}(t) \right] \\ & - (i/\hbar^2) \sum_j^{N_{\text{bath}}} \sum_{k=1}^{K_n} m_k^{(n)} \left(\alpha_k^{(n)} \mathbf{S}_n \rho_{\mathbf{m}_k^{-(n)}}(t) - \tilde{\alpha}_k^{(n)} \rho_{\mathbf{m}_k^{-(n)}}(t) \mathbf{S}_n \right) \quad , \quad (10) \end{aligned}$$

where $\mathbf{L}_S \bullet = -(i/\hbar) [\mathbf{H}_S, \bullet]$ is the Liouvillian ‘superoperator matrix representation’ of the system Hamiltonian matrix, \mathbf{S}_n are the matrices of the system operators of the n^{th} bath in the system-bath Hamiltonian \mathbf{H}_{SB} , and $\mathbf{m}_k^{\pm(n)} = \{m_1, \dots, m_k \pm 1, \dots, m_K\}$ are the indices of the ADOs for which the occupation number of one artificial mode of the n^{th} bath has been changed by one unit. Note that due to their definition in term of multi-integrals over time the ADOs have a dimension $[\text{time}]^{-L}$ where L is the hierarchy level^{66–69} given by the total occupation number of vector \mathbf{m} .

The hierarchy is thus structured in layers. Each level interacts only with the two neighboring layers. The Fourier transform (eq. (9)) provides analytical expressions of the α_k , $\tilde{\alpha}_k$, and $\gamma_k = \Omega_k + i\Gamma_k$ coefficients from the residue theorem, with the poles in the upper half plane^{70,71} when the spectral density is fitted by a sum of Tannor-Meier Lorentzian functions,⁶⁷

$$J(\omega) = \sum_{l=1}^{n_{\text{lor}}} \frac{p_l \omega}{\hbar^3 \left[(\omega + \Omega_l)^2 + \Gamma_l^2 \right] \left[(\omega - \Omega_l)^2 + \Gamma_l^2 \right]} \quad . \quad (11)$$

For each bath, the spectral density was fitted here in practice by a sum of three functions, $n_{\text{lor}} = 3$. The parameters of the Lorentzian functions are given in SI, table SI-I. Each Lorentzian leads to two artificial decay modes with oppo-

site frequencies, $\Omega_l + i\Gamma_l$ and $-\Omega_l + i\Gamma_l$. The corresponding weights, α_k , take into account the Bose function and satisfy the Boltzmann relation between system-bath absorption and emission. As already mentioned, the simulations provided here were made at room temperature. We neglect the poles coming from the Bose function that are called the Matsubara frequencies. Their consideration is crucial at very low temperature where their number becomes very large and requires different strategies to overcome the computational difficulties due to the prohibitive number of ADOs.^{71,72} The HEOM coupled equations were solved according to standard encoding within the adaptive Runge–Kutta method or within a tensor-train format, as described in refs.^{66,71}

2.3 Simulation of spectroscopic signals

We first present here the typical approaches based on linear-response theory to obtain the steady-state absorption and emission spectra, using the ML-MCTDH or HEOM formalisms. Then we summarize the main relations derived from the third-order optical response functions to simulate time-dependent spectroscopy with HEOM.^{36,37,73–79}

2.3.1 Steady-state absorption and emission spectroscopy

The linear-response steady-state absorption and emission spectra obtained with quantum wavepacket dynamics, here within the ML-MCTDH formalism, are typically computed as the power spectra of autocorrelation functions.

Let us define without loss of generality a molecular wavepacket within a (1+2)-manifold of diabatic electronic states (the ground state and two excited states) as a set of three components,

$$\Psi(\mathbf{Q}, t) = (\psi_0(\mathbf{Q}, t) \quad \psi_1(\mathbf{Q}, t) \quad \psi_2(\mathbf{Q}, t))^T \quad . \quad (12)$$

For a given initial state, $\Psi(t=0)$, we define the autocorrelation function as

$$c(t) = \langle \Psi(0) | \Psi(t) \rangle \quad , \quad (13)$$

where integration is performed over the nuclear degrees of freedom, \mathbf{Q} , according to standard Dirac’s bracket notations.

Unless otherwise specified, the so-called $t/2$ -trick can be used (always valid for a real-valued initial wavepacket and a Hermitian Hamiltonian, according to time-reversibility and unitary propagation),

$$c(t) = \langle \Psi(-t/2) | \Psi(t/2) \rangle \quad . \quad (14)$$

From an infinite propagation time, we should obtain the power spectrum associated to the propagation of this initial wavepacket upon taking the Fourier transform of the autocorrelation function,

$$\sigma(\omega) \propto \int_{-\infty}^{\infty} c(t) e^{i\omega t} dt \quad . \quad (15)$$

Because, numerically speaking, the final propagation time, t_f , is always finite, the autocorrelation function has to be

multiplied by some periodic and smoothly decaying function, for example $g(t) = \cos^n(\pi t/2t_f)$, in order to make the Fourier-transformed signal well-behaved and avoid the so-called Gibbs phenomenon over the finite time window ($n = 1$ in this work). An extra artificial dissipative broadening was also applied upon convoluting the spectra with a Lorentzian, hence multiplying the autocorrelation function with a damping function $\exp(-t/\tau)$, with an *ad hoc* damping time $\tau = 60$ fs corresponding to a half-width at half-maximum (HWHM) of 88 cm^{-1} , so as to mimic the numerical spectral widths effectively obtained from HEOM linear-response simulations of the same spectra (related to, but not to be confused with the Lorentzian HWHM parameter, $\Gamma = 160 \text{ cm}^{-1}$).

Such a time-to-energy procedure largely depends on how we define the initial state. For the absorption spectrum, we typically assume a sudden excitation of the ground-state vibrational wavefunction from the electronic ground state to each of the two electronic excited states. For the emission spectrum, the relaxed vibronic eigenstate within the excited state manifold must be computed beforehand. In a strongly-coupled and high-symmetrical situation such as in our previous work on the m22 dimer,⁵³ we could have considered each component of the superposition of the two vibrational contributions for each diabatic state and perhaps play with various mixtures. However, for m23, the electronic population ratio in the relaxed vibronic state is so close to one in the lowest diabatic state that we considered as a good approximation that we could reduce it to its single component in $D_1 \approx S_1$.

The customary state-to-state power spectra given in eq. (15) are independent of the transition dipole moments. They can be further summed with relative weights that reflect both transition dipole strengths so as to produce a total spectrum. This is here one of the main differences in computing linear spectra for the two approaches (wavepackets or reduced-density matrices), which is related to the way that the excitation is modelled. Within the HEOM description, the polarization of the electric field is included from the onset, so that all the electronic excited states having nonzero transition dipole moments are absorbing. Within the (ML-)MCTDH description, the polarization is not directly taken into account, and one has to decide from the onset which of the two electronic excited state is absorbing.

While such simulations based on wavepacket quantum dynamics and Fourier transforms are now routinely used for the simulation of steady-state spectroscopy, their extensions to nonlinear spectroscopies – requiring a third response formalism as in here – are becoming pressing matters. For instance, a recent and striking example of such an application based on the ML-MCTDH formalism can be found in ref.³³

Now, as regards HEOM, the absorption and emission spectra within linear response are written as follows (involving a ultimate over-the-system trace),

$$\sigma^{\text{abs}}(\omega) = \text{Re} \left\{ \text{FT} \left[\text{tr}_S \left(\rho_{\mu_+}^\dagger(t) \rho_{\mu_+}(0) \right) \right] \right\} \quad , \quad (16)$$

$$\sigma^{\text{em}}(\omega) = \text{Re} \left\{ \text{FT} \left[\text{tr}_S \left(\rho_{\mu_-}^\dagger(t) \rho_{\mu_-}(\text{eq}) \right) \right] \right\} \quad , \quad (17)$$

where the prefactor proportional to ω or ω^3 for absorption and emission, respectively, has been set equal to one for simplicity, and FT designates the Fourier transform.

The density matrices involved in them are built from the excitonic lowering and raising (transition-dipole) operators,

$$\mu_-^{(p)} = \sum_{j=1}^2 \mu_{0j,p} |0\rangle \langle j| \quad , \quad (18)$$

and

$$\mu_+^{(p)} = \sum_{j=1}^2 \mu_{0j,p} |j\rangle \langle 0| \quad , \quad (19)$$

where $p = x$ and $p = y$ denote the electric-field polarization directions along the x - or y -axes within the molecular plane (see fig. 1).

For the absorption, $\rho_{\mu_+}(0) = \sum_p \mu_+^{(p)} \rho_S(0)$ and all the ADOs are set to zero initially. For the emission, the lowering operator acts on the system density matrix $\rho_{\mu_-}(\text{eq}) = \sum_p \mu_-^{(p)} \rho_S(\text{eq})$ and on all the ADOs obtained when the equilibrium vibronic state within the excited electronic manifold – denoted eq – has been reached after relaxation. We consider different possibilities for the polarization: either parallel to the unit vectors e_x or e_y (see fig. 1), or also (for completion, since the definition of the two axes is quite arbitrary), along another oblique direction, along the unit vector $(e_x + e_y)/\sqrt{2}$. The first two cases will be referred to as XX and YY and lead to an initial condition with a superposed electronic state, $\mu_{01,x} |D_1\rangle + \mu_{02,x} |D_2\rangle$ or $\mu_{01,y} |D_1\rangle + \mu_{02,y} |D_2\rangle$. The oblique polarization, further denoted (X+Y)(X+Y), corresponds to the preparation of the superposed state $(\mu_{01,x} + \mu_{01,y}) |D_1\rangle + (\mu_{02,x} + \mu_{02,y}) |D_2\rangle$ (up to renormalization).

2.3.2 Time-resolved spectroscopy

We now expose the formal ingredients for the simulation of ideal time-frequency resolved spectra (in particular within the HEOM formalism) when assuming delta-like impulsive pump-probe laser pulses. We recall here the relations with the more general formalism of multi-time correlation functions, which are involved in nonlinear two-dimensional spectroscopy.²⁹

The third-order optical response function $R^{(3)}(t_3, t_2, t_1)$ that describes the system response to the light-induced perturbations is abundantly documented.^{28–34,41,80–82} The simulation of the 2D photon echo spectra involves the interaction between the system and four light pulses separated by three delay times as schematized in fig. 3.

The first pulse prepares a given optical coherence involving the excited states and the ground state. The following free evolution lasts for a time t_1 customarily called the coherence time. The second pulse creates a population in the excited manifold or in the ground state. The system then evolves freely during a time t_2 , which is the waiting or population time. The third pulse probes the system after this delay t_2 before a detection after the t_3 time interval. The third-order polarisation is then obtained by convolution with the laser pulses centered at τ_1 , τ_2 , and τ_3 , respectively (see fig. 3). They are each characterized by their polarization, wave vector k_n , frequency, envelope, and initial phase. Spec-

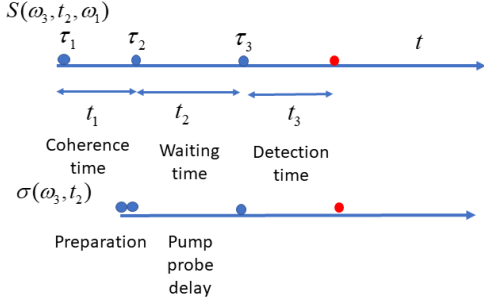


Figure 3: Scheme of principle of the three time intervals involved in the computation of 2D photon echo spectra involving Fourier transforms with respect to t_1 and t_3 or of the ESE (eq. (30)), GSB (eq. (31)), or TA (eq. (29)) spectra, for which $t_1 = 0$ and the Fourier transform is over t_3 .

tra derived from the response $R^{(3)}(t_3, t_2, t_1)$ without convolution with laser pulses are thus ideal spectra that would involve interactions with impulsive pulses described by delta distributions $\delta(t)$.

The system is initially in the ground state $|0\rangle$ and the bath is equilibrated at the reference FCP geometry at the chosen temperature T . By assuming a factorisation, the initial total density matrix is the product of the system density times the thermally equilibrated density of the bath $\rho_0 = \rho_S(0)\rho_{\text{eq}}(T)$. As extensively reviewed, the computation of $R^{(3)}(t_3, t_2, t_1)$ may be split into different responses that correspond to multi-time correlation functions and are associated to different processes: ESE (excited-state stimulated emission), GSB (ground-state bleaching), and ESA (excited-state absorption). The 2D signal involves six responses (for the sake of simplicity, the polarisation (p) is not written in the lowering or raising operators but it must be specified when using μ_- or μ_+),

$$R_1(t_3, t_2, t_1) = \langle \mu_- G(t_3) \{ G(t_2) [G(t_1) (\mu_+ \rho_0) \mu_-] \mu_+ \} \rangle, \quad (20)$$

$$R_2(t_3, t_2, t_1) = \langle \mu_- G(t_3) \{ G(t_2) [\mu_+ G(t_1) (\rho_0 \mu_-)] \mu_+ \} \rangle, \quad (21)$$

$$R_3(t_3, t_2, t_1) = \langle \mu_- G(t_3) \{ \mu_+ G(t_2) [G(t_1) (\rho_0 \mu_-) \mu_+] \} \rangle, \quad (22)$$

$$R_4(t_3, t_2, t_1) = \langle \mu_- G(t_3) \{ \mu_+ G(t_2) [\mu_- G(t_1) (\mu_+ \rho_0)] \} \rangle, \quad (23)$$

$$R_5(t_3, t_2, t_1) = \langle \mu_- G(t_3) \{ \mu_+ G(t_2) [\mu_+ G(t_1) (\rho_0 \mu_-)] \} \rangle, \quad (24)$$

$$R_6(t_3, t_2, t_1) = \langle \mu_- G(t_3) \{ \mu_+ G(t_2) [G(t_1) (\mu_+ \rho_0) \mu_-] \} \rangle. \quad (25)$$

The notation $\langle \bullet \rangle$ means here the trace over the system and the bath degrees of freedom, and $G(t)$ is the evolution operator in the full Liouville space. When the propagation is carried out with the HEOM method, the bath is represented by all the ADOs. The lowering or raising transition operators must be applied at each selected time to the system reduced-density matrix and to all the ADOs.³⁶

The first two responses, R_1 and R_2 , are associated to the ESE process, R_3 and R_4 describe GSB, while ESA is treated by R_5 and R_6 . The latter process is not considered here be-

cause the electronic basis set is truncated to the ground and the two D_1 and D_2 excited states. The total response function $R^{(3)}(t_3, t_2, t_1) = R_{\text{rp}}(t_3, t_2, t_1) + R_{\text{nr}}(t_3, t_2, t_1)$ for computing the 2D signal is the sum of two contributions, the rephasing one, R_{rp} (with detected wave vector $k = -k_1 + k_2 + k_3$), and the nonrephasing one, R_{nr} (with $k = k_1 - k_2 + k_3$). They are given as

$$\begin{aligned} R_{\text{rp}}(t_3, t_2, t_1) &= R_2(t_3, t_2, t_1) + R_3(t_3, t_2, t_1) - R_5(t_3, t_2, t_1) \quad , \\ R_{\text{nr}}(t_3, t_2, t_1) &= R_1(t_3, t_2, t_1) + R_4(t_3, t_2, t_1) - R_6(t_3, t_2, t_1) \quad . \end{aligned} \quad (26)$$

The 2D spectrum for a given waiting time t_2 is obtained by two Fourier transforms,

$$\begin{aligned} S(\omega_3, t_2, \omega_1) &= \text{Re} \int_0^\infty dt_1 \int_0^\infty dt_3 e^{i\omega_1 t_1 + i\omega_3 t_3} R_{\text{nr}}(t_3, t_2, t_1) \\ &+ \text{Re} \int_0^\infty dt_1 \int_0^\infty dt_3 e^{-i\omega_1 t_1 + i\omega_3 t_3} R_{\text{rp}}(t_3, t_2, t_1) \quad . \end{aligned} \quad (27)$$

The integral $\sigma(\omega_3, t_2) = \int_0^\infty S(\omega_3, t_2, \omega_1) d\omega_1$ is linked to the signal in the heterodyne transient grating or dispersed transient absorption (TA).⁴¹ By using eq. (27), it involves the responses for $t_1 = 0$,

$$\sigma(\omega_3, t_2) = \text{Re} \int_0^\infty dt_3 [R_{\text{nr}}(t_3, t_2, 0) + R_{\text{rp}}(t_3, t_2, 0)] e^{i\omega_3 t_3} \quad . \quad (28)$$

In all the expressions given in eqs. (20) to (23) with $t_1 = 0$, one has $G(t_1 = 0) = 1$, and the right part of the bracket describes the initial state that is assumed to be prepared by impulsive delta-like pulse associated to the lowering and raising operators. For ESE, this initial state, $\mu_+ \rho_0 \mu_-$, is the system reduced-density matrix of a superposition of the excited states weighted by the transition dipoles and leading to an unnormalized state, which may be normalized. All the ADOs are zero in the initial equilibrium baths. For GSB, $\rho_0 \mu_- \mu_+$ or $\mu_- \mu_+ \rho_0$ corresponds to the system ground state populated with the norm of the previous superposition and all ADOs nil.

The time t_2 takes the meaning of a delay between the pump and a probe. For the sake of convenience, the subscripts are removed and the time-dependent spectrum in eq. (28) is denoted $\sigma^{\text{TA}}(\omega, t)$. From eqs.(28) and (26), $\sigma^{\text{TA}}(\omega, t)$ may be split into two contributions (or three when ESA is not neglected). In our simulations, we get

$$\sigma^{\text{TA}}(\omega, t) = \sigma^{\text{ESE}}(\omega, t) + \sigma^{\text{GSB}}(\omega, t) \quad . \quad (29)$$

For $t_1 = 0$, one has $R_1(t_3, t_2, 0) = R_2(t_3, t_2, 0)$ and $R_3(t_3, t_2, 0) = R_4(t_3, t_2, 0)$, and the two contributions are finally given as

$$\sigma^{\text{ESE}}(\omega, t) = \text{Re} \int_0^\infty dt_3 e^{i\omega_3 t_3} R_1(t_3, t, 0) \quad , \quad (30)$$

$$\sigma^{\text{GSB}}(\omega, t) = \text{Re} \int_0^\infty dt_3 e^{i\omega_3 t_3} R_3(t_3, t, 0) \quad . \quad (31)$$

The GSB contribution does not depend on t_2 . Indeed, the system is prepared in the ground state and the correlation function computed after the excitation remains the same regardless of the waiting time. Thus, σ^{GSB} corresponds to the absorption spectrum of the linear response up to an arbitrary factor, which disappears when normalizing. Similarly, the ESE contribution evolves towards the stationary emission spectrum of the linear response when t_2 becomes sufficiently long. Using the $R_1(t_3, t, 0)$ response involves a specific initial state but the new equilibrated thermal state for long t_2 is in principle independent on the initial state. Both the absorption and emission spectra of the linear response are limiting cases of the time-dependent approach.

3 Results and discussion

3.1 EET dynamics

We first probe the characteristics of intramolecular EET within the m23 molecule by applying a sudden excitation from the ground state to the second electronic excited state. In practice, this is achieved upon initializing the system with the ground-state equilibrium wavepacket or reduced-density and placing it at $t = 0$ in the diabatic state localized on the p2 branch (D_2 , so-called donor state). From this initial state, the system is propagated within the excited-state manifold, allowing transfer to the diabatic state localized on the p3 branch (D_1 , so-called acceptor state). The electronic population transfer is shown in fig. 4 (left panel) for both ML-MCTDH and HEOM dynamics.

Population inversion occurs after around 20 fs in all types of simulations. Comparing the time evolution in the case of the LVC model only, we see that the population transfer calculated within the HEOM formalism is slightly slower than the one computed with a discrete definition of the modes (ML-MCTDH). The transfer is also more monotonic when using HEOM, which is due to the dissipative nature of the simulation, able to describe total relaxation. We also note that the more advanced case with eight hierarchy levels (L8) yields slightly delayed transfer dynamics compared to L7. This seems to be correlated with accounting for the small timelag due to the inflection feature around 10 fs, also observed in ML-MCTDH results.

The ML-MCTDH propagation has also been carried out with the more advanced LVC+ γ_{ii} and LVC+ γ models, which include second-order ‘‘intra-state couplings’’. The results are shown in fig. 4 (right panel) for longer timescales (up to 200 fs). The three models with the same propagation method (ML-MCTDH and similar ML-tree) exhibit small differences. The LVC model yields faster population transfer than the models including different curvatures (quadratic intra-state couplings) and mode mixing (bi-linear intra-state couplings). This, again, goes with a smaller timelag associated to a less pronounced inflection feature around 10 fs. After population inversion, the LVC model exhibits less stability once the acceptor state is populated (see around 75 fs and 150 fs for instance). The more we account for intra-state couplings (quadratic, LVC+ γ_{ii} and all bi-linear, LVC+ γ),

the more monotonic are the transfer to and the relaxation in the acceptor state.

The mode-mixing parameters slow down the population transfer dynamics but are eventually required to better relax toward the equilibrium geometry of the diabatic potential energy surfaces. This is consistent with a slightly stronger damping of the oscillatory features in the diabatic coherence, as shown in fig. 5. This means that the mode-mixing parameters somewhat enhance ‘‘internal dissipation’’ for the ML-MCTDH calculations, which is included from the onset in an *ad hoc* manner within the HEOM approach.

Again, we stress here that our estimation of the mode-mixing parameters is done thanks to the energy derivatives wrt. a large number of degrees of freedom. A more involved discussion of the importance of mode-mixing parameters, in particular as regards reducing dimensionality, is made in SI, section SI-I.

3.2 Steady-state spectroscopy

For ML-MCTDH, the exact same methodology as in a previous work for a reduced model is used to compute power spectra within the realm of steady-state (or linear) spectroscopy.⁴⁵ Two contributions, $\sigma^{(1)}(\omega)$ and $\sigma^{(2)}(\omega)$, are computed for the absorption spectrum (toward the D_1 and D_2 states, respectively) and one for the emission spectrum toward the ground state. In addition, we estimate the total absorption spectrum as

$$\begin{aligned} \sigma^{\text{Total}}(\omega) = & (\mu_{01,x}^2 + \mu_{01,y}^2) \sigma^{(1)}(\omega) \\ & + (\mu_{02,x}^2 + \mu_{02,y}^2) \sigma^{(2)}(\omega) \end{aligned} \quad (32)$$

which is further normalized. The weighting is isotropic as regards the polarization direction. It is also consistent with a sudden approximation for the excitation of both electronic excited states with electronic transition dipole strengths at the Franck-Condon point as effective weights for each contribution. They are all given in fig. 6 (left panel) for the LVC+ γ model.

Note that the emission spectrum is approximated as the power spectrum initialized with the most important vibrational contribution in the ground vibronic eigenstate of the excited state manifold (with more than 99% population in the D_1 electronic state) and projected to the electronic ground state.

The same is done in fig. 6 (center panel), obtained with the LVC model in order to compare with the HEOM linear-response calculations. Let us recall that the total absorption spectrum to both excited states with HEOM is obtained *a posteriori* by summing the spectra of the XX and YY cases so as to reproduce the weighting given in eq. (32). Both absorption and emission spectra compare well for the two methods. We observe a larger discrepancy in the spectral region after 4.0 eV, corresponding to the transitions toward the D_2 electronic excited state.

In fig. 6 (right panel), we now compare the results obtained by applying some specific oblique polarization (case

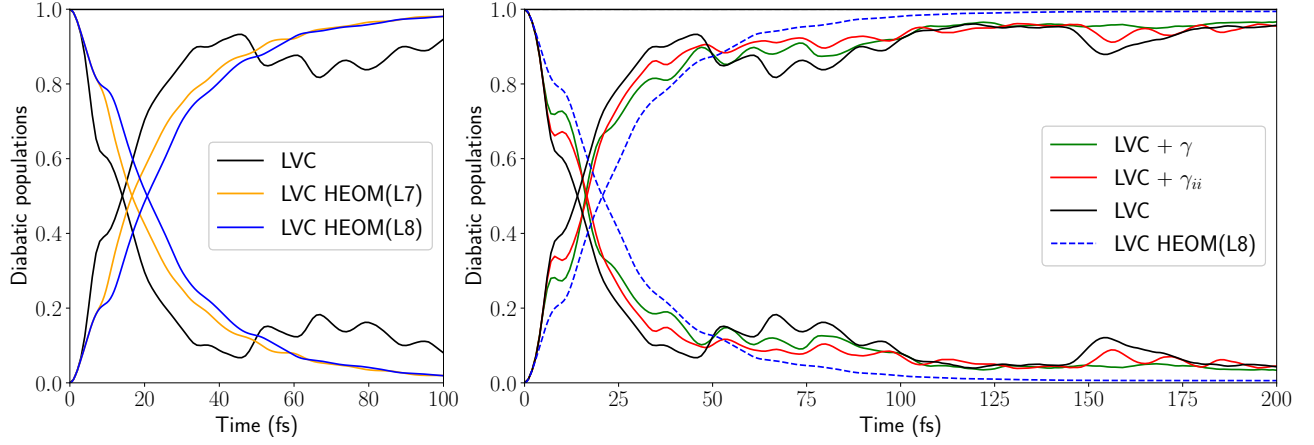


Figure 4: Diabatic populations for different models and propagation methods for the simulation of EET. Left: comparison of the use of the ML-MCTDH and HEOM (hierarchy levels L7 and L8) formalisms with the LVC model. Right: comparison of the use of the LVC, LVC+ γ_{ii} , and LVC+ γ models within the ML-MCTDH formalism, up to longer timescales.

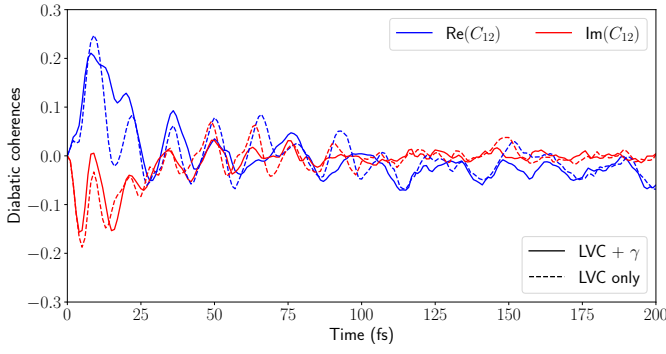


Figure 5: Real and imaginary parts (blue and red lines, respectively) of the diabatic coherence for the LVC+ γ and LVC only models, with plain and dashed lines, respectively.

(X+Y)(X+Y)) for checking its effect,

$$\begin{aligned} \sigma^{\text{Oblique}}(\omega) &= (\mu_{01,x} + \mu_{01,y})^2 \sigma^{(1)}(\omega) \\ &+ (\mu_{02,x} + \mu_{02,y})^2 \sigma^{(2)}(\omega) \end{aligned} \quad (33)$$

The oblique absorption spectrum, $\sigma^{\text{Oblique}}(\omega)$ is obtained with ML-MCTDH from the isolated spectra with weights in the sum that are different from the previous case, $\sigma^{\text{Total}}(\omega)$. With HEOM, the oblique spectra are computed from eq. (16) and eq. (17) with $\rho_{\mu_+}(0) = \sum_p \mu_+^{(p)} \rho_S(0)$ and ρ_{μ_-} (eq. = $\sum_p \mu_-^{(p)} \rho_S(\text{eq.})$, respectively, and the dipole operators given by eq. (18) and eq. (19).

The previously mentioned difference as regards absorption toward D_2 is even more remarkable for this numerical experiment. This is consistent with the fact that the y -polarized spectrum gives more importance to the absorption toward D_2 , which amplifies the effect of the discrepancy within this higher-energy spectral range.

In both approaches, we observe that the emission spectrum exhibits no Stokes shift. Both absorption and emission spectra overlap within a marked Lorentzian-like peak at the band origin 0-0. This is typical of very fast nuclear dynamics, which is to be expected when Mukamel's $\kappa = \Lambda/\Delta$ param-

eter²⁹ is larger than 1, where Λ^{-1} and Δ are estimates of the bath fluctuation timescale and of the amplitude of the fluctuations, respectively. With HEOM, Λ is taken as the spectral density cutoff and $\Delta = C^{1/2}(t=0)$ is given by the squareroot of the initial value of the bath correlation function.⁶⁶

While the spectra generated with ML-MCTDH or HEOM match only qualitatively, their comparison remains much satisfactory in view of the great differences between both approaches. Each discrete mode of the LVC model is enlarged according to a uniform and quite arbitrary manner (eq.(6)). A more relevant simulation of the spectral densities would take the dynamics of the environment into account, as done for example in refs.^{59-61,83,84} Also, the fit with only three Tannor-Meier Lorentzian functions (eq.(11)) to reduce the computational time is not perfect, and the tuning baths are assumed to be uncorrelated. One may also invoke some temperature effects since the MCTDH is at 0 K and HEOM at room temperature.

3.3 Toward nonlinear/time-resolved spectroscopies

The computation of the nonlinear response (eq. (20)), to obtain the ESE contribution (eq. (30)) requires a two-dimensional (t_2, t_3)-grid. The t_2 domain is chosen to probe the early nonadiabatic dynamics during 150 fs. The t_3 -range spans 300 fs. It is fixed to ensure enough decay of the correlation function before the Fourier transform. The timestep is 0.24 fs (10 a.u.). A full grid can be computed with a reasonable computational time by taking into account only the two peaks at high frequencies for each spectral density shown in fig. 2. This approximation, which retains only two Lorentzian functions in eq. (11), is called the 2L model while the full model is referred to as the 3L model. The 2L model involves four artificial decay modes for each spectral density. Each HEOM propagation then requires 50,388 ADOs at level 7 of the HEOM hierarchy. In contrast, computations with the 3L model involve 480,700 ADOs at the same level, and only some cuts for selected delay times t_2 have been performed in the 3L model.

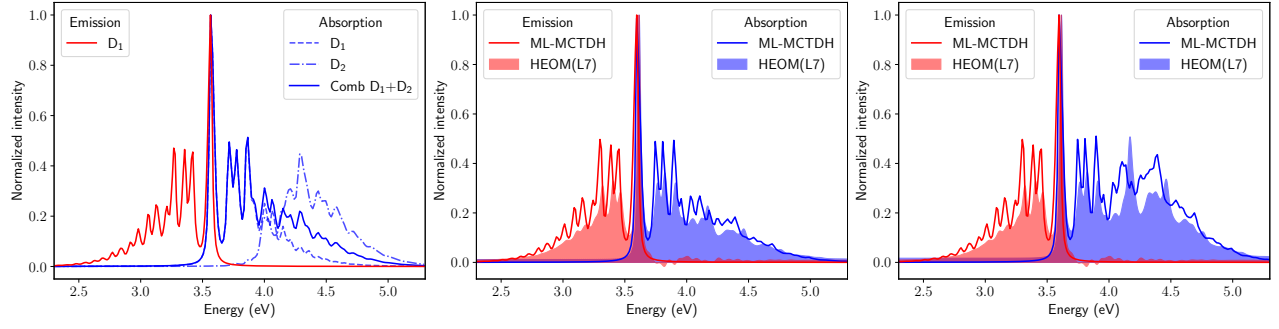


Figure 6: Individual or combined contributions to the absorption spectra from the ground state to D_1 , D_2 , or both: dashed blue, dotted blue, and plain blue, respectively. Emission spectra from the vibronic ground state within the excited (D_1 , D_2) manifold: plain red line. The ML-MCTDH spectra are broadened by using a damped autocorrelation function with damping time $\tau = 60$ fs. The HEOM spectra are displayed as filled spectra for the sake of visibility. Left: ML-MCTDH spectra for the LVC+ γ model. Center: ML-MCTDH and HEOM spectra for the LVC model with dipole strength ponderation, eq. (32). Right: ML-MCTDH and HEOM spectra for the LVC model with a ponderation corresponding to an electric field along an oblique polarisation (case $(X+Y)(X+Y)$), eq. (33).

We consider that the pump at $t_1 = 0$ and the probe after t_2 have the same polarization, either parallel to vector e_x (case XX) or e_y (case YY), or along an oblique direction $(e_x + e_y)/\sqrt{2}$ (case $(X+Y)(X+Y)$) (see fig. 1). Due to the transition dipole strengths, the XX case mainly populates the D_1 state, implying excitation of the p_3 branch. In contrast, the YY case excites both states with similar weights, such that the D_2 state can give rise to EET to D_1 .

Figure 7 presents time-and-energy-resolved spectrograms of ESE (eq. (30)) (left panels) and TA (eq. (29)) (right panels) for the 2L model obtained with a sampling of 9 delay times t_2 with time step 0.24 fs (10 a.u.) up to 2.4 fs followed by 50 values with step 2.4 fs. The TA spectrograms are the sum of the ESE and GSB contributions. As discussed in section 2.3.2, the GSB contribution does not depend on t_2 and simply adds up the absorption spectrum for the chosen polarization at all times.

The ESE evolution during the early dynamics is more visible when comparing different cuts through the spectrograms for selected delays that are indicated by vertical dashed lines. The time-resolved cuts obtained for the full 3L model are given in fig. 8. They are given in SI, fig. SI-8, in the case of the 2L model for comparison, showing similar qualitative behavior. Cuts through the TA spectrograms are also given in SI, figs. SI-9 and SI-10, for both the 3L and 2L models.

For very short delays, ESE corresponds to the absorption spectrum. It is due to stimulated Rabi oscillations at the frequencies of the vertical transitions from the equilibrium ground state. As soon as the propagation begins, the energy gap varies and the ADOs are gradually populated. The application of the transition dipole operators at t_2 affects all the ADOs. Around $t_2 = 2.5$ fs, Fano profiles (abrupt changes from positive to negative intensities) appear due to interferences in the optical response between bath and system.^{85,86} These particular profiles are not a signature of the nonadiabatic interaction since they persist in the D_1 or D_2 states when the inter-state coupling is artificially suppressed (see SI, fig. SI-14). For a longer delay, one sees the turnover from the absorptive to the emissive profile that reaches its

asymptotic value after about 125 fs.

Figure 9 illustrates the strong evolution of the ESE and TA profiles for the next-to-initial time (0.2 fs) and the long time (121 fs) close to the equilibrium. The GSB spectrum, which remains the same at all times, is drawn in dotted lines. For the very short delay, ESE and GSB are the same when the pump and probe pulses have the same polarization. The TA signal is then twice the GSB spectrum. For the long delay, the TA signal becomes equal to the GSB one in the range of the absorption spectrum since ESE becomes negligible in this domain. On the contrary, TA coincides with ESE in the range of the stationary emission spectrum. This suggests that the ESE time-dependent signal can be obtained from the time-dependent TA signal upon subtracting from it half of the initial TA spectrum, which is equivalent to the GSB contribution, at least when the polarizations are identical.

3.4 EET spectral fingerprints

In this section, we illustrate how some features of the ideal impulsive pump-probe spectra may be related to EET dynamics. We first consider the evolution of some peak intensities (horizontal cuts through the spectrograms) and then we analyse the integrated signal over the range of frequencies.

Figure 10 gives the ESE intensity at two frequencies corresponding to the main transitions to state D_1 (p_3 branch) or D_2 (p_2 branch) at 3.681 eV and 4.241 eV, respectively. They are horizontal slices through the ESE spectrogram for the 2L model but the behavior is similar to that of the 3L model as may be seen by following the maximum of the peaks in fig. 8. When the polarization is along e_x (fig. 10, left panel), ESE concerns the evolution in D_1 that gives rise to a negligible inter-state transition. On the contrary, a signature of EET may be seen when following the ESE for the transition at 4.241 eV with the polarization along e_y (fig. 10, right panel). Indeed, the initial signal at 4.241 eV completely disappears in about 20 fs.

We now examine how a more global fingerprint of EET dynamics may be found in the ESE signal $S^{\text{ESE}}(t)$ obtained

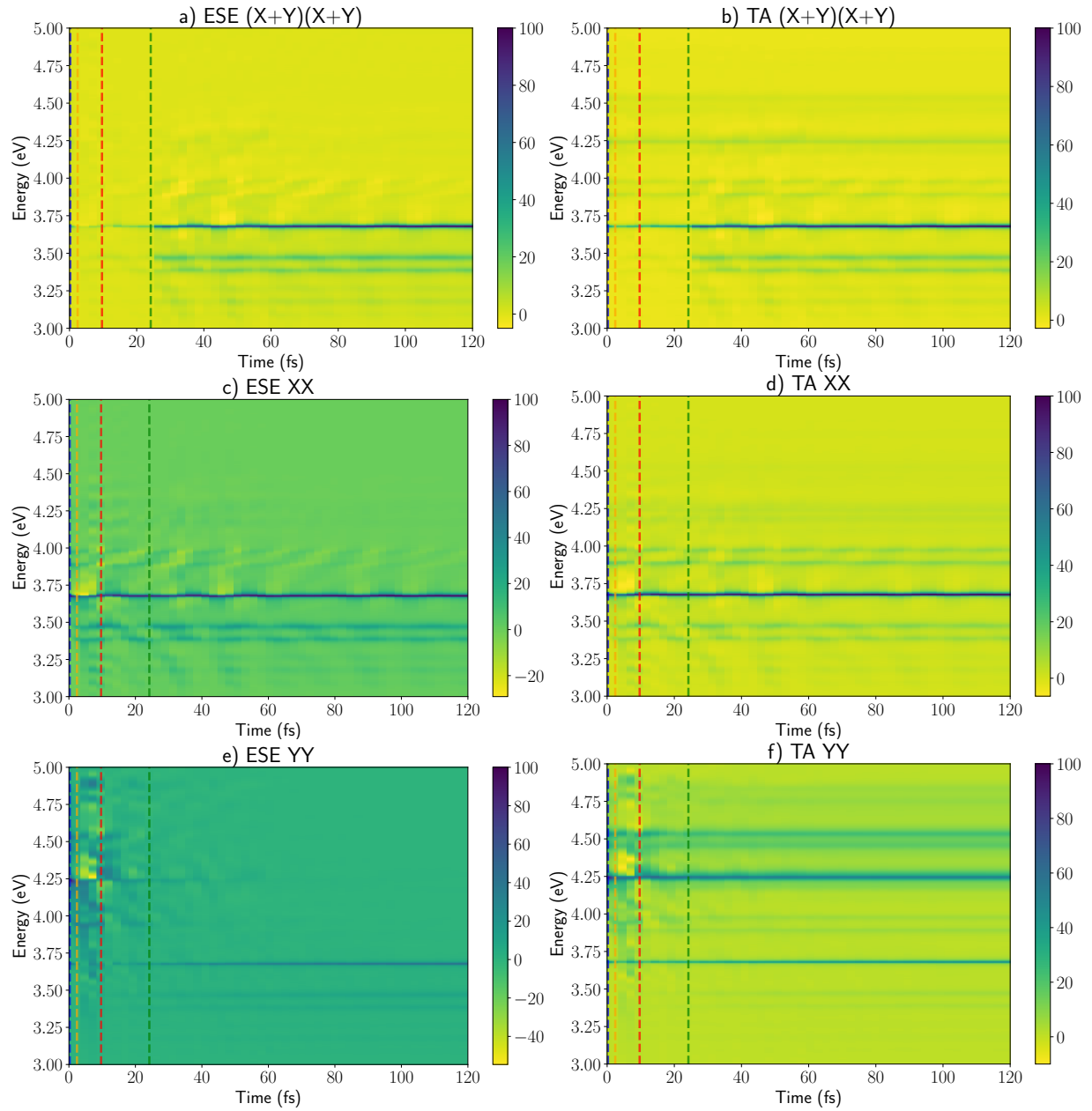


Figure 7: Time-and-frequency-resolved ESE (left panels) and TA (right panels) spectrograms (eqs. (29) and (30)) for the approximate 2L model with only the two high-frequency peaks in the spectral densities of fig. 2. The pump and probe are delta-like laser pulses. The polarizations are along $(e_x + e_y)/\sqrt{2}$ (top), e_x (middle), and e_y (bottom). The vertical dashed lines indicate the cuts presented in fig. 8 for the full 3L model, and in SI, fig. SI-8 for the 2L model.

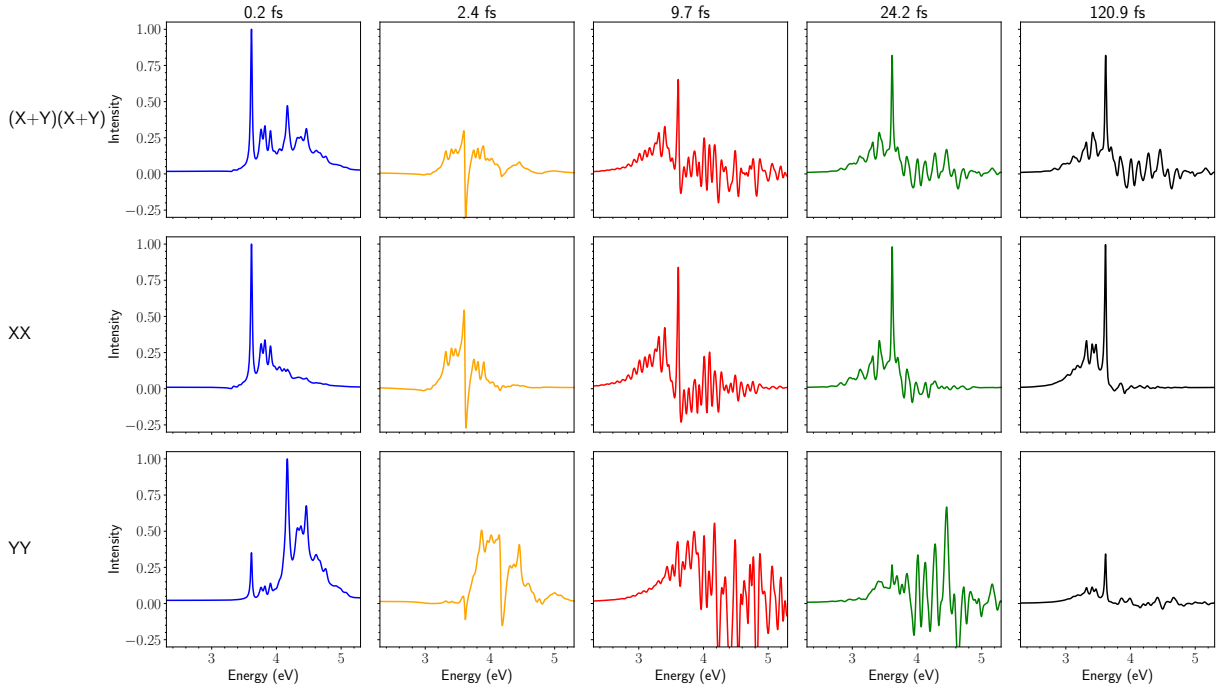


Figure 8: Cuts through the time- and frequency-resolved ESE spectrograms for different pump-probe delays shown in dashed lines in fig. 7 obtained in the case of the full 3L model. The corresponding cuts with the 2L model are given in SI, fig. SI-8. The polarizations are along $(e_x + e_y)/\sqrt{2}$ (top), e_x (middle), and e_y (bottom). The spectra are normalized with the maximum intensity among spectra along the same line (with the same polarization).

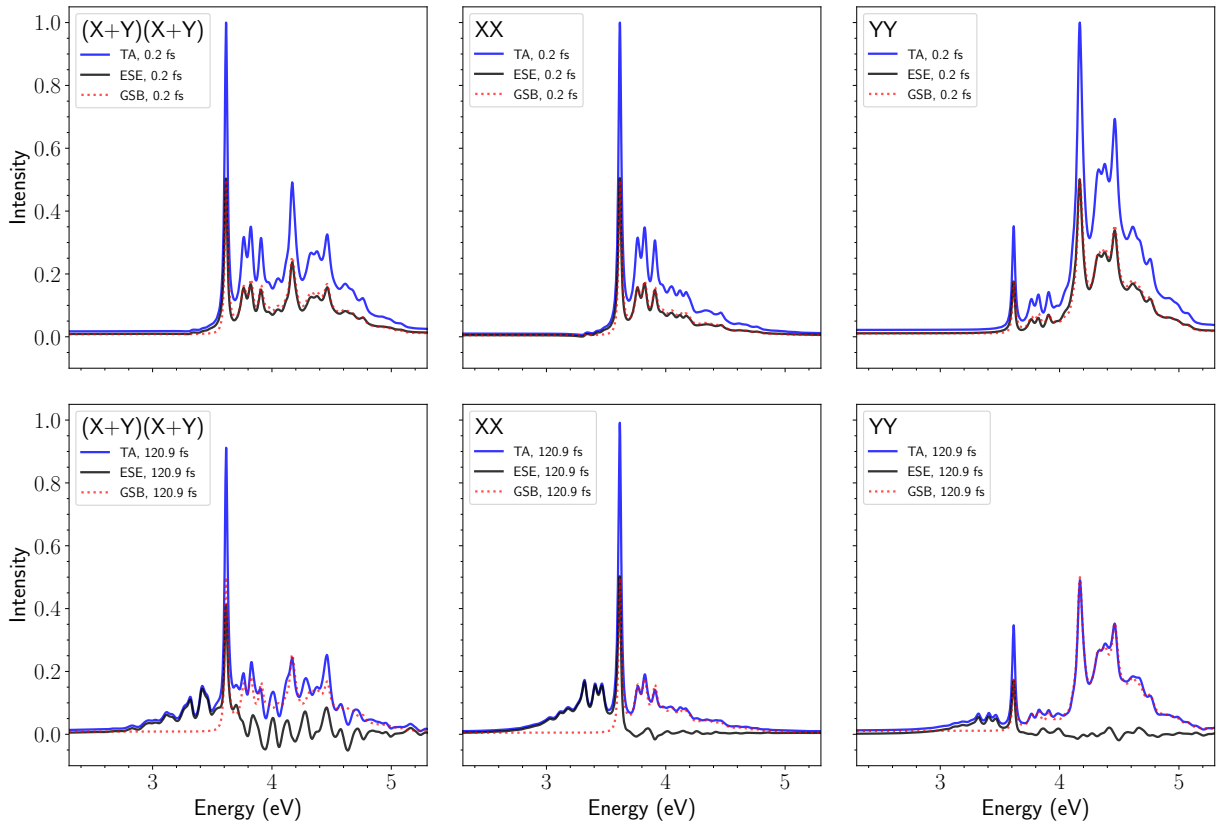


Figure 9: ESE and TA signals obtained within the 3L model at 0.2 fs and 120.9 fs, compared with GSB (constant at all times). From left to right, the polarizations are along $(e_x + e_y)/\sqrt{2}$, e_x , and e_y . The spectra are normalized with the maximum intensity among spectra in the same column (with the same polarization).

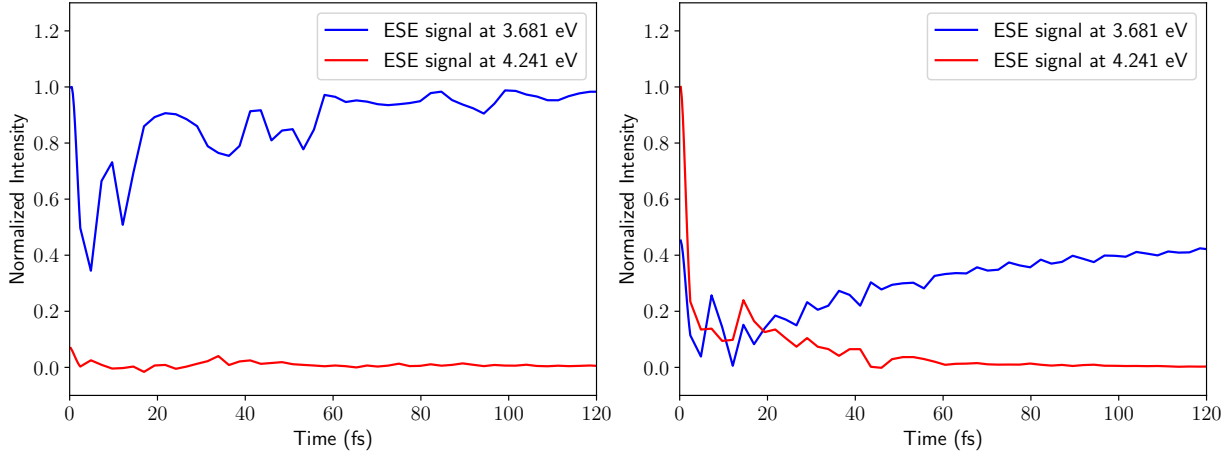


Figure 10: Time-resolved slices through the ESE spectrogram (eq. (30)) at two different frequencies corresponding to maxima in the steady-state absorption spectrum. Left panel: polarization along e_x , right panel: polarization along e_y .

upon integrating $\sigma^{\text{ESE}}(\omega, t)$ (eq. (30)) over the frequency domain. $S^{\text{ESE}}(t)$ gives the area of the emission spectrum and due to the Fourier transform relation it is given by the response $R_1(t_3 = 0, t, 0)$ for $t_3 = 0$. We consider four situations, some of which are fictitious cases without inter-state coupling, in order to dissect the various influences on the signal $S^{\text{ESE}}(t)$.

(i) Only one state, D_1 (case XX) or D_2 (case YY), is excited by approximating the transition dipoles to their largest components only ($\mu_{01} \approx (-4.77, 0, 0)$ a.u., $\mu_{02} \approx (0, 2.01, 0)$ a.u.) and assuming that there is no inter-state coupling. The initial electronic state is then stationary. Hence, the initial value $R_1(t_3 = 0, t, 0)$ does not depend on t even if the response for $t_3 \neq 0$ depends on t . Thus, $S^{\text{ESE}}(t)$ remains constant, and the shape of the ESE spectrum evolves with preserving its area. Indeed, for any delay t_2 , the density matrix remains constant with a single population $P_j = 1$ ($j = 1$ or 2). The application of μ_+ after the delay t_2 creates an optical coherence $\rho_{S,j0}$ (between the electronic system states j and 0) that is also independent of t_2 . At the end of t_3 , μ_- projects this coherent superposition into the ground state.

(ii) The two states D_1 and D_2 are excited in the XX or YY cases ($\mu_{01} = (-4.77, 0.80, 0)$ a.u., $\mu_{02} = (1.84, 2.01, 0)$ a.u.), and the inter-state coupling is nil. The initial electronic state is then a superposition with an initial electronic coherence but the populations remain constant. This is called a pure dephasing case of the electronic system, induced by the vibrational bath in each state. The left panel of fig. 11 compares the evolution of $S^{\text{ESE}}(t)$ for the two polarizations XX and YY with the decoherence function of a field-free case given by the relative modulus of the electronic coherence $\tilde{C}(t) = |\rho_{S,12}(t)|/|\rho_{S,12}(0)|$. One observes that $S^{\text{ESE}}(t)$ now exhibits a fast initial decay with a rate similar to that of the (de)coherence function. $S^{\text{ESE}}(t)$ then becomes nearly constant as in the previous case when the coherence becomes negligible. In this situation, even if the populations are not varying, the electronic coherence strongly depends on the delay t_2 due to the effect of the tuning baths. The action of μ_+ at that time generates different optical coherences $\rho_{S,j0}$ ($j = 1, 2$), and the projection into the ground state after t_3 is

different for each delay as long as the coherence evolves.

(iii) Similar to case (i) but the inter-state coupling now operates. The middle panel of fig. 11 illustrates the remarkable behavior of $S^{\text{ESE}}(t)$ that follows the evolution of the populations, in particular the decay of the most excited state. The evolution of the reduced-density matrix before the application of μ_+ is now due to the variation of the populations that are transformed to optical coherences and projected by μ_- after t_3 with a yield that evolves with the same rate as the population decay. After normalizing to disregard the value of the transition dipole, the $S^{\text{ESE}}(t)$ signal perfectly follows the population decay due to the inter-state coupling.

(iv) Similar to case (ii) but accounting for the inter-state coupling. This is the most realistic situation. It is shown in fig. 11, right panel. $S^{\text{ESE}}(t)$ now contains fingerprints of both the decoherence and the EET population transfer. The (de)coherence function presents a similar initial decay as in case (ii) but is damped by the population transfer. In the YY case, the most populated state is D_2 . Unlike the case without coupling displayed in the left panel, $S^{\text{ESE}}(t)$ now continues to decrease and the rate of decay is very similar to that of the D_2 state shown in dashed-dotted line (the initial populations, $P_1 = 0.13$ and $P_2 = 0.87$, are fixed by the normalized superposed state prepared at $t_1 = 0$). In the XX case, the behavior of $S^{\text{ESE}}(t)$ is quite similar to that without coupling but it stabilizes to a higher value. Again the slight increase follows the evolution of the D_1 population, shown in dashed line (the initial populations are $P_1 = 0.86$ and $P_2 = 0.14$). Hence, case (iv) is a mixture of cases (ii) and (iii) as regards the time evolution of the $S^{\text{ESE}}(t)$ signal. While it may be difficult to disentangle the two effects in practice, our numerical experiments thus provide a guideline for deciphering the relative roles played by decoherence and EET when probing the time-resolved spectroscopy of an optically active manifold of two vibronically coupled excited electronic states that can be excited coherently by the pump. For the sake of completion, non-normalized signals are provided in SI, fig. SI-13.

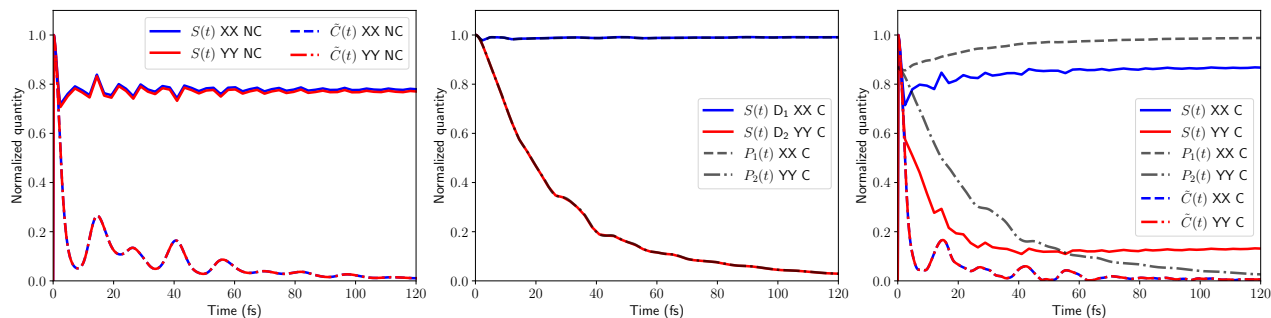


Figure 11: Normalized integrated ESE signal, $S(t) = S^{\text{ESE}}(t)$, relative modulus of the electronic coherence, $\tilde{C}(t) = |\rho_{S,12}(t)|/|\rho_{S,12}(0)|$, and electronic populations, $P_1(t)$, $P_2(t)$, in a field-free situation (when assuming the initial preparation). From left to right: cases (ii), (iii), and (iv), such as discussed in section 3.4. In the case (ii): coherently superposed electronic state without inter-state coupling (NC), case (iii): single initial electronic state with inter-state coupling (C), and case (iv): coherently superposed electronic state with inter-state coupling (C). Note that (1,2)-populations are constant with time in case (ii), and the (1,2)-coherence in case (iii), which is why they are not plotted.

4 Conclusions and outlook

The first focus of the present work was to extend to high dimensionality and/or dissipative approaches our previous reduced-dimensionality study of ultrafast EET occurring in the smallest asymmetrical *meta*-substituted PPE oligomer, m23, made of 2-ring (p2) and 3-ring (p3) *para*-substituted pseudo-fragments.⁴⁵

As regards this prototypical system, the donor state is mainly localized on p2 and the acceptor state on p3. For the isolated m23 system, we have constructed an *ab initio* high-dimensional vibronic coupling Hamiltonian (VCH) model for the first two singlet electronic excited states accounting for all the 93 in-plane vibrational degrees of freedom in terms of a linear vibronic coupling (LVC) model and various types of quadratic vibronic coupling (QVC) extensions.

Wavepacket simulations using a 93-dimensional ML-MCTDH approach confirmed a typical timescale of about 25 fs for intramolecular EET, which was confirmed with the dissipative reduced-density approach known as HEOM. The primary role of the high-frequency acetylenic and quinoidal vibrations was confirmed.

The second focus of our work was to investigate the time-dependent non linear spectroscopy with particular attention paid to TA spectra as regards their GSB and ESE components. Highlighting the role of the high-frequency modes in ML-MCDTH simulations allowed us to retain only the essential parts of the spectral densities and generate 2D spectrograms, which deserve some care so as not to become too computationally expensive.

All the nonlinear spectra presented here correspond to ideal impulsive delta-like laser pulses, and some fingerprints of EET have been characterized in this context. A more realistic description of such phenomena remains awaited, both on the theoretical and experimental fronts.

Acknowledgments

J. G. acknowledges the French MESR (Ministère de l'Enseignement supérieur, de la Recherche) and the ENS (Ecole Normale Supérieure) of Lyon for funding his PhD grant, hosted at the University of Montpellier.

Supporting information

Supporting information are provided. It includes: a discussion on bilinear terms in VCH models, a representation of the ML-MCTDH wavefunction, additional information on nuclear displacements, on spectral densities, and on bath dynamics in HEOM, additional figures for the discussion of nonlinear spectroscopy.

References

- (1) Xu, Z.; Moore, J. S. Design and synthesis of a convergent and directional molecular antenna. *Acta Polymerica* **1994**, *45*, 83–87.
- (2) Devadoss, C.; Bharathi, P.; Moore, J. S. Energy transfer in dendritic macromolecules: molecular size effects and the role of an energy gradient. *Journal of the American Chemical Society* **1996**, *118*, 9635–9644.
- (3) Shortreed, M. R.; Swallen, S. F.; Shi, Z.-Y.; Tan, W.; Xu, Z.; Devadoss, C.; Moore, J. S.; Kopelman, R. Directed energy transfer funnels in dendrimeric antenna supermolecules. *The Journal of Physical Chemistry B* **1997**, *101*, 6318–6322.
- (4) Melinger, J. S.; Pan, Y.; Kleiman, V. D.; Peng, Z.; Davis, B. L.; McMorro, D.; Lu, M. Optical and photophysical properties of light-harvesting phenylacetylene monodendrons based on unsymmetrical branching. *Journal of the American Chemical Society* **2002**, *124*, 12002–12012.
- (5) Swallen, S. F.; Kopelman, R.; Moore, J. S.; Devadoss, C. Dendrimer photoantenna supermolecules: energetic funnels, exciton hopping and correlated excimer formation. *Journal of Molecular Structure* **1999**, *485-486*, 585–597.
- (6) Kopelman, R.; Shortreed, M.; Shi, Z.-Y.; Tan, W.; Xu, Z.; Moore, J. S.; Bar-Haim, A.; Klafter, J. Spectroscopic evidence for excitonic localization in fractal antenna supermolecules. *Physical Review Letters* **1997**, *78*, 1239–1242.
- (7) Minami, T.; Tretiak, S.; Chernyak, V.; Mukamel, S. Frenkel-exciton Hamiltonian for dendrimeric nanostar. *Journal of Luminescence* **2000**, *87-89*, 115–118.
- (8) Chernyak, V.; Minami, T.; Mukamel, S. Exciton transport in molecular aggregates probed by time and frequency gated optical spectroscopy. *The Journal of Chemical Physics* **2000**, *112*, 7953–7963.
- (9) Heller, E. J. Time-dependent approach to semiclassical dynamics. *The Journal of Chemical Physics* **1975**, *62*, 1544–1555.
- (10) Meyer, H. D.; Manthe, U.; Cederbaum, L. S. The multi-configurational time-dependent Hartree approach. *Chemical Physics Letters* **1990**, *165*, 73–78.
- (11) Beck, M. H.; Jäckle, A.; Worth, G. A.; Meyer, H. D. The multiconfiguration time-dependent Hartree (MCTDH) method: a Highly efficient algorithm for propagating wavepackets. *Physics Reports* **2000**, *324*, 1–105.
- (12) Raab, A.; Worth, G.; Meyer, H.-D.; Cederbaum, L. Molecular dynamics of pyrazine after excitation to the S₂ electronic state using a realistic 24-mode model Hamiltonian. *The Journal of Chemical Physics* **1999**, *110*, 936–946.
- (13) Cattarius, C.; Worth, G. A.; Meyer, H.-D.; Cederbaum, L. S. All mode dynamics at the conical intersection of an octa-atomic molecule: Multi-configuration time-dependent Hartree (MCTDH) investigation on the butatriene cation. *The Journal of Chemical Physics* **2001**, *115*, 2088–2100.
- (14) Wang, H.; Thoss, M. Multilayer formulation of the multiconfiguration time-dependent Hartree theory. *The Journal of Chemical Physics* **2003**, *119*, 1289–1299.
- (15) Manthe, U. A multilayer multiconfigurational time-dependent Hartree approach for quantum dynamics on general potential energy surfaces. *The Journal of Chemical Physics* **2008**, *128*, 164116.
- (16) Wang, H. Multilayer multiconfiguration time-dependent Hartree theory. *The Journal of Physical Chemistry A* **2015**, *119*, 7951–7965.
- (17) Zewail, A. H. Femtochemistry: Recent Progress in Studies of Dynamics and Control of Reactions and Their Transition States. *The Journal of Physical Chemistry* **1996**, *100*, 12701–12724.
- (18) Tully, J. C.; Preston, R. K. Trajectory surface hopping approach to nonadiabatic molecular collisions: the reaction of H⁺ with D₂. *The Journal of Chemical Physics* **1971**, *55*, 562–572.
- (19) Tully, J. C. Molecular dynamics with electronic transitions. *The Journal of Chemical Physics* **1990**, *93*, 1061–1071.
- (20) Lasorne, B.; Worth, G. A.; Robb, M. A. Excited-state dynamics. *WIREs Computational Molecular Science* **2011**, *1*, 460–475.
- (21) Crespo-Otero, R.; Barbatti, M. Recent advances and perspectives on nonadiabatic mixed quantum–classical dynamics. *Chemical Reviews* **2018**, *118*, 7026–7068.
- (22) Agostini, F.; Curchod, B. F. E. Different flavors of nonadiabatic molecular dynamics. *WIREs Computational Molecular Science* **2019**, *9*, e1417.
- (23) Casida, M.; Huix-Rotllant, M. Progress in time-dependent density-functional theory. *Annual Review of Physical Chemistry* **2012**, *63*, 287–323.
- (24) Gross, E. K. U.; Maitra, N. T. *Fundamentals of Time-Dependent Density Functional Theory*; Lecture Notes in Physics; Springer, 2012; pp 53–99.

- (25) Barone, V.; Bloino, J.; Biczysko, M.; Santoro, F. Fully integrated approach to compute vibrationally resolved optical spectra: From small molecules to macrosystems. *Journal of Chemical Theory and Computation* **2009**, *5*, 540–554.
- (26) Santoro, F.; Improta, R.; Lami, A.; Bloino, J.; Barone, V. Effective method to compute Franck-Condon integrals for optical spectra of large molecules in solution. *The Journal of Chemical Physics* **2007**, *126*, 084509.
- (27) Santoro, F.; Lami, A.; Improta, R.; Bloino, J.; Barone, V. Effective method for the computation of optical spectra of large molecules at finite temperature including the Duschinsky and Herzberg–Teller effect: The Qx band of porphyrin as a case study. *The Journal of Chemical Physics* **2008**, *128*, 224311.
- (28) Cho, M.; Scherer, N. F.; Fleming, G. R.; Mukamel, S. Photon echoes and related four-wave-mixing spectroscopies using phase-locked pulses. *The Journal of Chemical Physics* **1992**, *96*, 5618–5629.
- (29) Mukamel, S. *Principles of nonlinear optical spectroscopy*; Oxford University Press, 1995.
- (30) Kowalewski, M.; Fingerhut, B. P.; Dorfman, K. E.; Bennett, K.; Mukamel, S. Simulating Coherent Multidimensional Spectroscopy of Nonadiabatic Molecular Processes: From the Infrared to the X-ray Regime. *Chemical Reviews* **2017**, *117*, 12165–12226.
- (31) Collini, E. 2D Electronic Spectroscopic Techniques for Quantum Technology Applications. *The Journal of Physical Chemistry C* **2021**, *125*, 13096–13108.
- (32) Rose, P. A.; Krich, J. J. Automatic Feynman diagram generation for nonlinear optical spectroscopies and application to fifth-order spectroscopy with pulse overlaps. *The Journal of Chemical Physics* **2021**, *154*, 034109.
- (33) Segatta, F.; Aranda, D.; Aleotti, F.; Montorsi, F.; Mukamel, S.; Garavelli, M.; Santoro, F.; Nenov, A. Time-resolved x-ray absorption spectroscopy: an MCTDH quantum dynamics protocol. *Journal of Chemical Theory and Computation* **2023**,
- (34) Shah, S.; Li, H.; Bittner, E. R.; Silva, C.; Piryatinski, A. QuDPy: A Python-based tool for computing ultrafast non-linear optical responses. *Computer Physics Communications* **2023**, *292*, 108891.
- (35) Tanimura, Y.; Kubo, R. Time Evolution of a Quantum System in Contact with a Nearly Gaussian-Markoffian Noise Bath. *J. Phys. Soc. Jpn.* **1989**, *58*, 101–114.
- (36) Tanimura, Y. Stochastic Liouville, Langevin, Fokker–Planck, and Master Equation Approaches to Quantum Dissipative Systems. *Journal of the Physical Society of Japan* **2006**, *75*, 082001.
- (37) Tanimura, Y. Numerically “exact” approach to open quantum dynamics: The hierarchical equations of motion (HEOM). *J. Chem. Phys.* **2020**, *153*, 020901.
- (38) Xu, R.-X.; Yan, Y. Dynamics of quantum dissipation systems interacting with bosonic canonical bath: Hierarchical equations of motion approach. *Phys. Rev. E* **2007**, *75*, 031107.
- (39) Shi, Q.; Chen, L.; Nan, G.; Xu, R.-X.; Yan, Y. Efficient Hierarchical Liouville Space Propagator to Quantum Dissipative Dynamics. *J. Chem. Phys.* **2009**, *130*, 084105.
- (40) Bai, S.; Zhang, S.; Huang, C.; Shi, Q. Hierarchical Equations of Motion for Quantum Chemical Dynamics: Recent Methodology Developments and Applications. *Accounts of Chemical Research* **2024**, *57*, 3151–3160.
- (41) Sun, K.; Huang, Z.; Gelin, M. F.; Chen, L.; Zhao, Y. Monitoring of singlet fission via two-dimensional photon-echo and transient-absorption spectroscopy: Simulations by multiple Davydov trial states. *The Journal of Chemical Physics* **2019**, *151*, 114102.
- (42) Joo, T.; Jia, Y.; Yu, J.; Lang, M. J.; Fleming, G. R. Third-order nonlinear time domain probes of solvation dynamics. *The Journal of Chemical Physics* **1996**, *104*, 6089–6108.
- (43) Fernandez-Alberti, S.; Kleiman, V. D.; Tretiak, S.; Roitberg, A. E. Nonadiabatic molecular dynamics simulations of the energy transfer between building blocks in a phenylene ethynylene dendrimer. *The Journal of Physical Chemistry A* **2009**, *113*, 7535–7542.
- (44) Huang, J.; Du, L.; Hu, D.; Lan, Z. Theoretical analysis of excited states and energy transfer mechanism in conjugated dendrimers. *Journal of Computational Chemistry* **2015**, *36*, 151–163.
- (45) Galiana, J.; Lasorne, B. Excitation energy transfer and vibronic relaxation through light-harvesting dendrimer building blocks: A nonadiabatic perspective. *The Journal of Chemical Physics* **2024**, *160*, 104104.
- (46) Malone, W.; Nebgen, B.; White, A.; Zhang, Y.; Song, H.; Bjorggaard, J. A.; Sifain, A. E.; Rodriguez-Hernandez, B.; Freixas, V. M.; Fernandez-Alberti, S.; Roitberg, A. E.; Nelson, T. R.; Tretiak, S. NEXMD software package for nonadiabatic excited state molecular dynamics simulations. *Journal of Chemical Theory and Computation* **2020**, *16*, 5771–5783.
- (47) Fernandez-Alberti, S.; Makhov, D. V.; Tretiak, S.; Shalashilin, D. V. Non-adiabatic excited state molecular dynamics of phenylene ethynylene dendrimer using a multiconfigurational Ehrenfest approach. *Physical Chemistry Chemical Physics* **2016**, *18*, 10028–10040.

- (48) Hu, D.; Peng, J.; Chen, L.; Gelin, M. F.; Lan, Z. Spectral fingerprint of excited-state energy transfer in dendrimers through polarization-sensitive transient-absorption pump–probe signals: On-the-fly nonadiabatic dynamics simulations. *The Journal of Physical Chemistry Letters* **2021**, *12*, 9710–9719.
- (49) Liu, S.; Peng, J.; Bao, P.; Shi, Q.; Lan, Z. Ultrafast Excited-State Energy Transfer in Phenylene Ethynylene Dendrimer: Quantum Dynamics with the Tensor Network Method. *The Journal of Physical Chemistry A* **2024**.
- (50) Frisch, M. J.; Trucks, G. W.; Schlegel, H. B.; Scuseria, G. E.; Robb, M. A.; Cheeseman, J. R.; Scalmani, G.; Barone, V.; Petersson, G. A.; Nakatsuji, H.; Li, X.; Caricato, M.; Marenich, A. V.; Bloino, J.; Janesko, B. G.; Gomperts, R.; Mennucci, B.; Hratchian, H. P.; Ortiz, J. V.; Izmaylov, A. F.; Sonnenberg, J. L.; Williams-Young, D.; Ding, F.; Lipparini, F.; Egidi, F.; Goings, J.; Peng, B.; Petrone, A.; Henderson, T.; Ranasinghe, D.; Zakrzewski, V. G.; Gao, J.; Rega, N.; Zheng, G.; Liang, W.; Hada, M.; Ehara, M.; Toyota, K.; Fukuda, R.; Hasegawa, J.; Ishida, M.; Nakajima, T.; Honda, Y.; Kitao, O.; Nakai, H.; Vreven, T.; Throssell, K.; Montgomery, J. A., Jr.; Peralta, J. E.; Ogliaro, F.; Bearpark, M. J.; Heyd, J. J.; Brothers, E. N.; Kudin, K. N.; Staroverov, V. N.; Keith, T. A.; Kobayashi, R.; Normand, J.; Raghavachari, K.; Rendell, A. P.; Burant, J. C.; Iyengar, S. S.; Tomasi, J.; Cossi, M.; Millam, J. M.; Klene, M.; Adamo, C.; Cammi, R.; Ochterski, J. W.; Martin, R. L.; Morokuma, K.; Farkas, O.; Foresman, J. B.; Fox, D. J. Gaussian 16 Revision A.03. 2016.
- (51) Ho, E. K. L.; Lasorne, B. Diabatic pseudofragmentation and nonadiabatic excitation-energy transfer in meta-substituted dendrimer building blocks. *Computational and Theoretical Chemistry* **2019**, *1156*, 25–36.
- (52) Fernandez-Alberti, S.; Kleiman, V. D.; Tretiak, S.; Roitberg, A. E. Unidirectional energy transfer in conjugated molecules: the crucial role of high-frequency C(triple)C bonds. *The Journal of Physical Chemistry Letters* **2010**, *1*, 2699–2704.
- (53) Galiana, J.; Lasorne, B. On the unusual Stokes shift in the smallest PPE dendrimer building block: Role of the vibronic symmetry on the band origin? *The Journal of Chemical Physics* **2023**, *158*, 124113.
- (54) Gonon, B.; Lasorne, B.; Karras, G.; Joubert-Doriol, L.; Lauvergnat, D.; Billard, F.; Lavorel, B.; Faucher, O.; Guérin, S.; Hertz, E.; Gatti, F. A generalized vibronic-coupling Hamiltonian for molecules without symmetry: Application to the photoisomerization of benzopyran. *The Journal of Chemical Physics* **2019**, *150*, 124109.
- (55) Gonon, B.; Perveaux, A.; Gatti, F.; Lauvergnat, D.; Lasorne, B. On the applicability of a wavefunction-free, energy-based procedure for generating first-order nonadiabatic couplings around conical intersections. *The Journal of Chemical Physics* **2017**, *147*, 114114.
- (56) Breuer, H.-P.; Petruccione, F. *The Theory of Open Quantum Systems*; Oxford University Press, 2002.
- (57) Weiss, U. *Quantum Dissipative Systems*; Singapore, World Scientific, 2012.
- (58) May, V.; Kühn, O. *Charge and Energy Transfer Dynamics in Molecular Systems*; John Wiley and Sons, Ltd, 2011.
- (59) Mangaud, E.; de la Lande, A.; Meier, C.; Desouter-Lecomte, M. Electron transfer within a reaction path model calibrated by constrained DFT calculations: application to mixed-valence organic compounds. *Phys. Chem. Chem. Phys.* **2015**, *17*, 30889–30903.
- (60) Tong, Z.; Gao, X.; Cheung, M. S.; Dunietz, B. D.; Geva, E.; Sun, X. Charge transfer rate constants for the carotenoid-porphyrin-C60 molecular triad dissolved in tetrahydrofuran: The spin-boson model vs the linearized semiclassical approximation. *J. Chem. Phys.* **2020**, *153*, 044105.
- (61) Dunnett, A. J.; Gowland, D.; Isborn, C. M.; Chin, A. W.; Zuehlsdorff, T. J. Influence of nonadiabatic effects on linear absorption spectra in the condensed phase: Methylene blue. *J. Chem. Phys.* **2021**, *155*, 144112.
- (62) Martinazzo, R.; Hughes, K. H.; Martelli, F.; Burghardt, I. Effective Spectral Densities for System-Environment Dynamics at Conical Intersections: S2–S1 Conical Intersection in Pyrazine. *Chem. Phys.* **2010**, *377*, 21 – 29.
- (63) Tamura, H.; Martinazzo, R.; Ruckebauer, M.; Burghardt, I. Quantum Dynamics of Ultrafast Charge Transfer at an Oligothiophene-Fullerene Heterojunction. *J. Chem. Phys.* **2012**, *137*, 22A540.
- (64) Woods, M. P.; Groux, R.; Chin, A. W.; Huelga, S. F.; Plenio, M. B. Mappings of open quantum systems onto chain representations and Markovian embeddings. *J. Math. Phys.* **2014**, *55*, 032101.
- (65) Worth, G. A.; Giri, K.; Richings, G. W.; Burghardt, I.; Beck, M. H.; Jäckle, A.; Meyer, H. D. The quantum package, version 2.0, University of Birmingham; Birmingham, UK. 2020.
- (66) Mangaud, E.; Jaouadi, A.; Chin, A.; Desouter-Lecomte, M. Survey of the hierarchical equations of motion in tensor-train format for non-Markovian quantum dynamics. *Eur. Phys. J. Spec. Top.* **2023**, *232*, 1847–1869.

- (67) Meier, C.; Tannor, D. J. Non-Markovian Evolution of the Density Operator in the Presence of Strong Laser Fields. *J. Chem. Phys.* **1999**, *111*, 3365–3376.
- (68) Ishizaki, A.; Fleming, G. R. Unified Treatment of Quantum Coherent and Incoherent Hopping Dynamics in Electronic Energy Transfer: Reduced Hierarchy Equation Approach. *J. Chem. Phys.* **2009**, *130*, 234111.
- (69) Ishizaki, A.; Calhoun, T. R.; Schlau-Cohen, G. S.; Fleming, G. R. Quantum coherence and its interplay with protein environments in photosynthetic electronic energy transfer. *Phys. Chem. Chem. Phys.* **2010**, *12*, 7319–7337.
- (70) Pomyalov, A.; Meier, C.; Tannor, D. J. The Importance of Initial Correlations in Rate Dynamics: A Consistent Non-Markovian Master Equation Approach. *Chem. Phys.* **2010**, *370*, 98–108.
- (71) Le Dé, B.; Jaouadi, A.; Mangaud, E.; Chin, A. W.; Desouter-Lecomte, M. Managing temperature in open quantum systems strongly coupled with structured environments. *The Journal of Chemical Physics* **2024**, *160*, 244102.
- (72) Xu, M.; Yan, Y.; Shi, Q.; Ankerhold, J.; Stockburger, J. T. Taming Quantum Noise for Efficient Low Temperature Simulations of Open Quantum Systems. *Phys. Rev. Lett.* **2022**, *129*, 230601.
- (73) Ishizaki, A.; Tanimura, Y. Multidimensional vibrational spectroscopy for tunneling processes in a dissipative environment. *The Journal of Chemical Physics* **2005**, *123*, 014503.
- (74) Tanimura, Y. Reduced hierarchy equations of motion approach with Drude plus Brownian spectral distribution: Probing electron transfer processes by means of two-dimensional correlation spectroscopy. *The Journal of Chemical Physics* **2012**, *137*, 22A550.
- (75) Chen, L.; Zheng, R.; Shi, Q.; Yan, Y. Two-dimensional electronic spectra from the hierarchical equations of motion method: Application to model dimers. *The Journal of Chemical Physics* **2010**, *132*, 024505.
- (76) Zhu, K.-B.; Xu, R.-X.; Zhang, H. Y.; Hu, J.; Yan, Y. J. Hierarchical Dynamics of Correlated System-Environment Coherence and Optical Spectroscopy. *The Journal of Physical Chemistry B* **2011**, *115*, 5678–5684.
- (77) Chen, L.; Zheng, R.; Jing, Y.; Shi, Q. Simulation of the two-dimensional electronic spectra of the Fenna-Matthews-Olson complex using the hierarchical equations of motion method. *The Journal of Chemical Physics* **2011**, *134*, 194508.
- (78) Yan, Y.; Liu, Y.; Xing, T.; Shi, Q. Theoretical study of excitation energy transfer and nonlinear spectroscopy of photosynthetic light-harvesting complexes using the nonperturbative reduced dynamics method. *WIREs Computational Molecular Science* **2021**, *11*, e1498.
- (79) Fetherolf, J. H.; Berkelbach, T. C. Linear and nonlinear spectroscopy from quantum master equations. *The Journal of Chemical Physics* **2017**, *147*, 244109.
- (80) Khalil, M.; Demirdöven, N.; Tokmakoff, A. Coherent 2D IR Spectroscopy: Molecular Structure and Dynamics in Solution. *The Journal of Physical Chemistry A* **2003**, *107*, 5258–5279.
- (81) Abramavicius, D.; Palmieri, B.; Voronine, D. V.; Šanda, F.; Mukamel, S. Coherent Multidimensional Optical Spectroscopy of Excitons in Molecular Aggregates; Quasiparticle versus Supermolecule Perspectives. *Chemical Reviews* **2009**, *169*, 2350–2408.
- (82) Krčmář, J.; Gelin, M. F.; Domcke, W. Simulation of femtosecond two-dimensional electronic spectra of conical intersections. *The Journal of Chemical Physics* **2015**, *143*, 074308.
- (83) Hunter, K. E.; Mao, Y.; Chin, A. W.; Zuehlsdorff, T. J. Environmentally Driven Symmetry Breaking Quenches Dual Fluorescence in Proflavine. *The Journal of Physical Chemistry Letters* **2024**, *15*, 4623–4632.
- (84) Lambertson, E.; Bashirova, D.; Hunter, K. E.; Hansen, B.; Zuehlsdorff, T. J. Computing linear optical spectra in the presence of nonadiabatic effects on graphics processing units using molecular dynamics and tensor-network approaches. *The Journal of Chemical Physics* **2024**, *161*, 114101.
- (85) Zhang, H.-D.; Yan, Y. Onsets of hierarchy truncation and self-consistent Born approximation with quantum mechanics prescriptions invariance. *The Journal of Chemical Physics* **2015**, *143*, 214112.
- (86) Finkelstein-Shapiro, D.; Poulsen, F.; Pullerits, T. o.; Hansen, T. Coherent two-dimensional spectroscopy of a Fano model. *Phys. Rev. B* **2016**, *94*, 205137.

Supplementary Information to:
Wavepacket and Reduced-Density Approaches
for High-Dimensional Quantum Dynamics:
Application to the Nonlinear Spectroscopy of
Asymmetrical Light-Harvesting Building
Blocks

Joachim Galiana,^{†,¶} Michèle Desouter-Lecomte,[‡] and Benjamin Lasorne^{*,†}

[†]*ICGM, Univ Montpellier, CNRS, ENSCM, Montpellier, France*

[‡]*Institut de Chimie Physique, Université Paris-Saclay-CNRS, UMR8000, F-91400 Orsay, France*

[¶]*Current affiliation: Departamento de Química, Universidad Autónoma de Madrid, Madrid,
Spain*

E-mail: benjamin.lasorne@umontpellier.fr

Contents

1	A note on bilinear terms and VCH reduced models	2
2	ML-MCTDH wavefunction	5
3	Nuclear displacements: discrete modes	6
4	Spectral densities	7

5	Bath dynamics in HEOM	9
6	Nonlinear spectroscopy	11
6.1	Additional cuts and slices through the ESE and TA spectrograms	11
6.2	ESE signals in the uncoupled case	13
	References	15

1 A note on bilinear terms and VCH reduced models

The adiabatic Hessians, diabatic Hessians, and γ -matrices are given in the first three columns of fig. 1. The terms selected in the LVC+ γ model are shown in the fourth column of fig. 1.

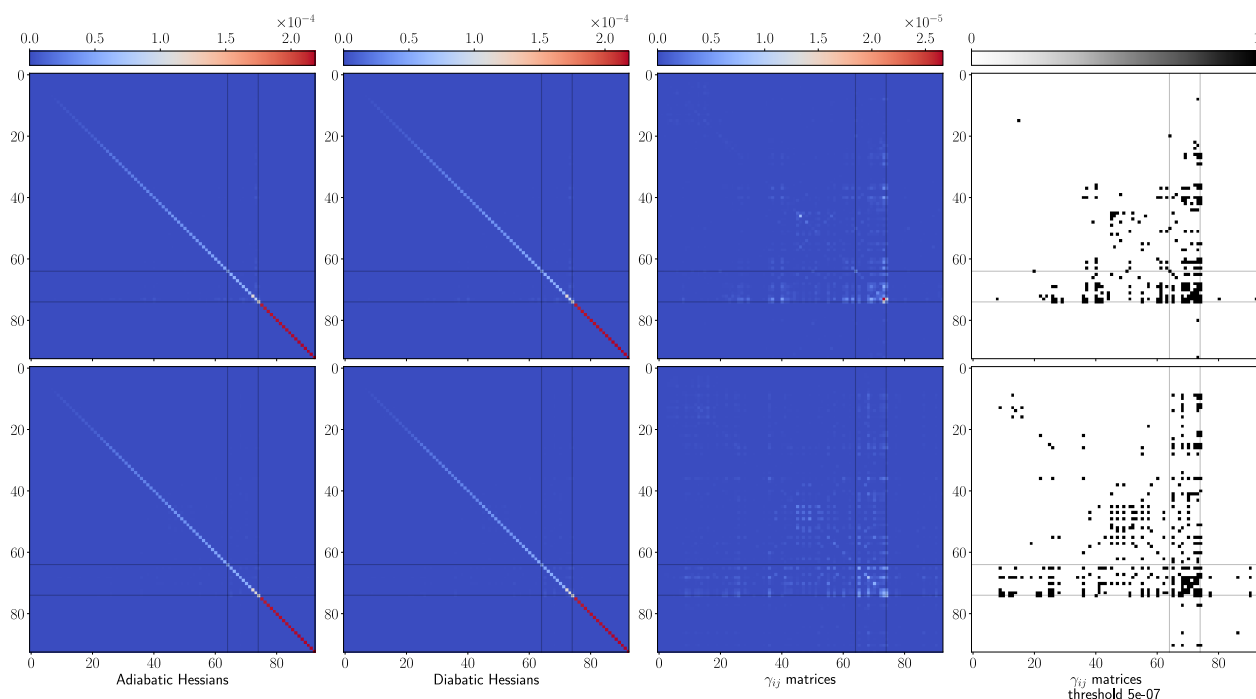


Figure 1: From left to right, absolute values of the: i) adiabatic Hessians \mathbf{K}_S of S_1 and S_2 at the the FC geometry (FCP); ii) post-processed diabatic Hessians \mathbf{K}_D of D_1 and D_2 at FCP; iii) mode-mixing matrices $\gamma^{(s)} = \mathbf{K}_{D_s} - \mathbf{K}_{S_0}$ for the two electronic states; iv) same with blanks where values are $\leq 5 \times 10^{-7} \frac{E_h}{a_0^2 m_e}$ (unselected values). All Hessians are projected onto the normal modes computed at FCP. The top and bottom panels correspond to the first and second excited states, respectively. The grey horizontal and vertical lines define the region of quinooidal, anti-quinooidal, and acetylenic normal modes.

The relevance of the γ -matrices for a dimensionally-reduced model is detailed hereafter. We compare the EET dynamics simulated for the LVC model parametrized *via* a global fit (fitting of *ab initio* PESs, see Ref. ¹), to the LVC-parametrized model *via* a local fit (identification of energy derivatives; this work). For such a comparison, we extract the 8-dimensional *child* model from the 93-dimensional *parent* model, upon freezing all the unselected normal modes in quantum-dynamics calculations.

We show in fig. 2 the population transfer dynamics of EET for simulations for which the matrices $\gamma_{ij,i\neq j}$ are smoothly switched on from 0 (blue lines) to 1 (gray lines), and to 2 (red lines).⁴

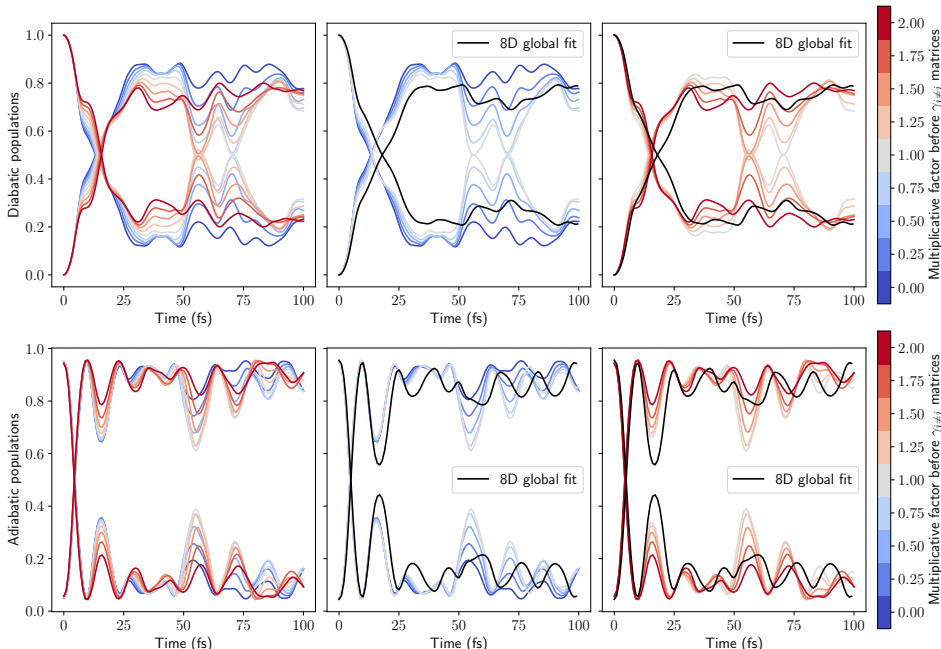


Figure 2: Diabatic and adiabatic populations (top and bottom panels, respectively) of the first two excited states for various LVC models. The results obtained when varying the off-diagonal bilinear matrices from 0 (LVC model with different curvatures for the excited states but no mode mixing) to $\gamma_{i\neq j}$ (same but with actual mode mixing) [left and center panels], and from $\gamma_{i\neq j}$ to $2\gamma_{i\neq j}$ (artificially enhanced mode mixing) [left and right panels] are shown with a colormap from blue to red as regards the multiplicative factor. The results obtained with the 8D global fit are shown in black lines for comparison [center and right panels].

For both diabatic and adiabatic populations, the early EET population transfer (up to 50 fs) seems to be only slightly affected by the variations of the $\gamma_{ij,i\neq j}$ -matrices. In particular, we note that the diabatic population transfer is slightly faster when switching on, and enhancing, the mode

mixing.

This is likely due to the contribution of the $\gamma_{j,i \neq j}$ -parameters to the diabatic gradient difference, which really drives the early dynamics. Quite counter-intuitively, the diabatic quantum yield (again, before 50 fs) is higher for simulations with no mode mixing, while we would expect bilinear intra-state couplings to allow for more efficient relaxations in the S_1 electronic state. For longer times, we observe that the diabatic states mix again with a 50:50 population ratio for the case of $1 \times \gamma_{ij}$, at both 55 fs and 70 fs.

Quite counter-intuitively again, the transfer is more monotonic in the extreme case of $0 \times \gamma_{ij}$ than in the (supposedly more realistic) case of $1 \times \gamma_{ij}$. A plausible explanation would be that accounting for the mode mixing *via* non-zero bilinear intra-state couplings is not accurate enough in low-dimensional systems. Indeed, as we have observed above, with the same model ($1 \times \gamma_{ij}$), but without freezing any in-plane mode, there is no diabatic recrossing. The same is found for the extreme case of $2 \times \gamma_{ij}$, which is an artificial enhancement of mode-mixing parameters.

Our interpretation is that accounting for mode mixing (that is, intra-state bilinear couplings), *via* a local fit of the excited-state Hessians, might not be adapted to low-dimensional models. Indeed, with the *a priori* more realistic local fit parametrization ($1 \times \gamma_{ij}$), the results are significantly different from the global fit parametrization. This can be explained by the fact that the γ_{ij} -parameters are obtained for the full-dimensional system, so that they might take too much importance when used in a reduced model.

We note that these effects are not found to the same extent in the adiabatic population transfer, although the simulation of EET with $1 \times \gamma_{ij}$ also exhibits significant recrossings at 55 fs and 70 fs.

2 ML-MCTDH wavefunction

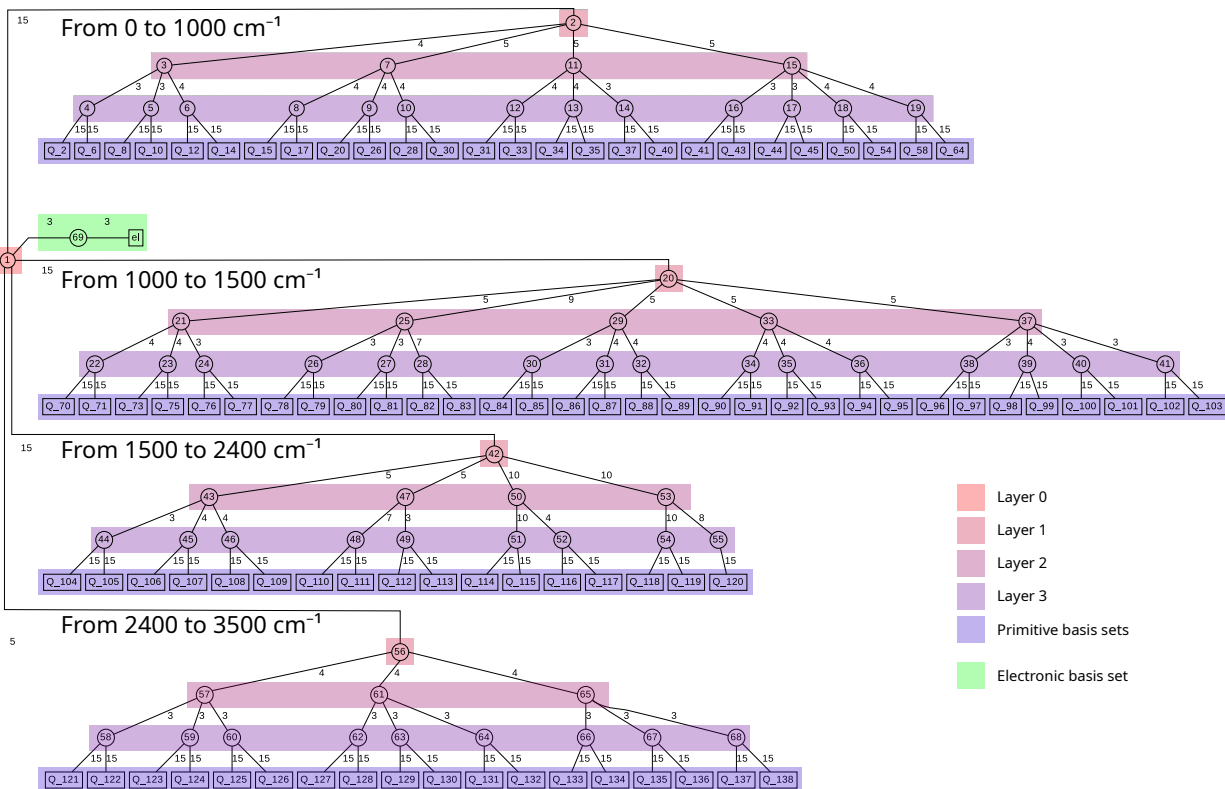


Figure 3: Representation of the ML-tree used for the quantum-dynamics simulations with the (1+2)-state 93-dimensional LVC model. The layer for the electronic states is given in green. The layers for the vibrational degrees of freedom are given in red to blue shading, from the top layer to the primitive basis, respectively. Nodes are in circles, primitive modes are in squares. The size of the basis set for each expansion (nodes or modes) is given above the corresponding node.

3 Nuclear displacements: discrete modes

As studied in previous work,¹ intramolecular EET can be characterized by following the geometry of the molecule (here, the expectation values of positional operators, see fig. 4), or the vibronic relaxations (vibrational energy per mode and per state, see fig. 5, relative to the energy within the electronic system at FCP).

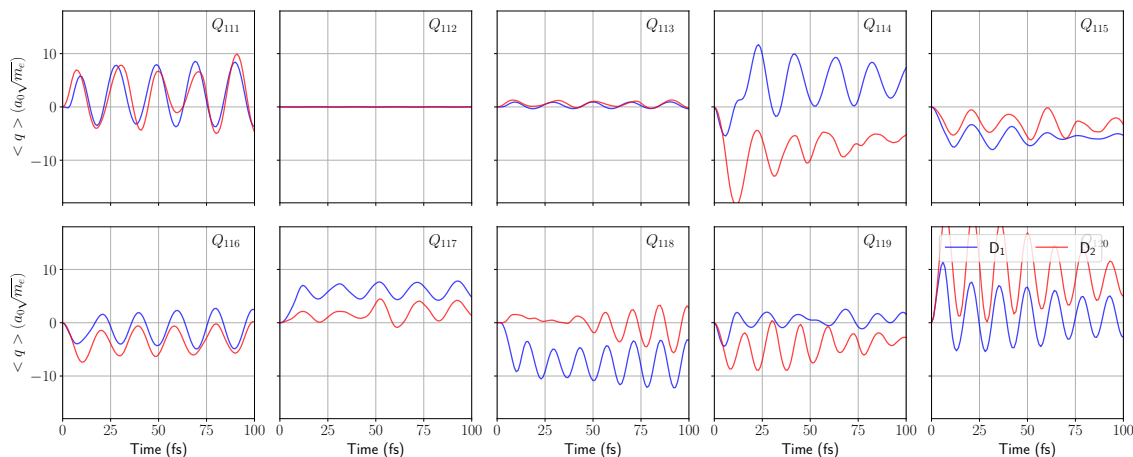


Figure 4: Time evolution of the state-specific expectation values of the position operator in diabatic states D_1 and D_2 for a selection of normal modes of vibration among the 93-dimensional model. The expectation values are computed with the propagated ML-MCTDH wavepacket for the LVC+ γ model after initial excitation to D_2 .

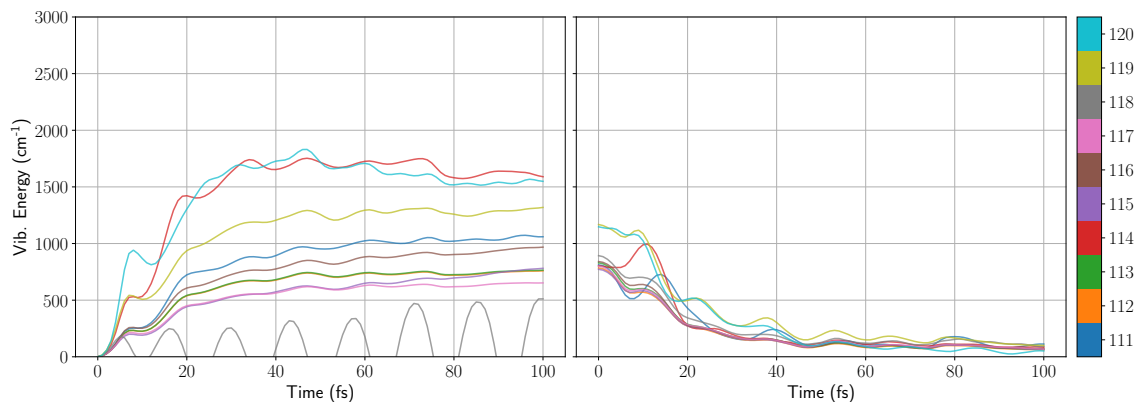


Figure 5: Time evolution of the vibrational energy per mode (for a selection of modes among the 93-dimensional model) and per state, (D_1 or D_2 , left and right, respectively), calculated with the propagated ML-MCTDH wavepacket for the LVC+ γ model after initial excitation to D_2 .

4 Spectral densities

The spectral densities using the LVC parameters are given as,

$$J_n(\omega) = \frac{\pi}{2} \sum_k \frac{f_k^{(n)2}}{\omega_k} \delta(\omega - \omega_k) \quad . \quad (1)$$

They only involve the intramolecular vibrations. In order to account for the existence of an environment, the delta distribution is broadened by a Lorentzian smoothing function,

$$\delta(\omega - \omega_j) \sim \frac{1}{\pi} \frac{\Gamma}{(\omega - \omega_j)^2 + \Gamma^2} \quad , \quad (2)$$

leading to a continuous spectral density shown in fig. 6. We take $\Gamma = 160 \text{cm}^{-1}$ (HWHM).

The spectral density of each tuning or coupling bath is fitted by a sum of n_{lor} Tannor-Meier Lorentzian functions,^{2,3}

$$J^{\text{TM}}(\omega) \approx \sum_{l=1}^{n_{\text{lor}}} \frac{p_l \omega}{\hbar^3 \left[(\omega + \Omega_l)^2 + \Gamma_l^2 \right] \left[(\omega - \Omega_l)^2 + \Gamma_l^2 \right]} \quad . \quad (3)$$

The parameters p_l , Ω_l , and Γ_l are given in Table 1.

Table 1: Parameters of the Tannor-Meier Lorentzian functions fitting the spectral densities of the three-bath model. $J_1(\omega)$ and $J_2(\omega)$ correspond to the tuning bath that makes the relative energies of states D_1 and D_2 fluctuate to first order (tuning). $J_3(\omega)$ refers to the coupling bath inducing first-order variations of the interstate coupling.

	p_l (Ha ⁴)	$\hbar\Omega_l$ (Ha)	$\hbar\Gamma_l$ (Ha)
J_1	5.5×10^{-10}	1.078687×10^{-2}	3.40×10^{-4}
	3.3×10^{-10}	7.6634×10^{-3}	4.0×10^{-4}
	1.5×10^{-10}	5.4517×10^{-3}	5.0×10^{-4}
J_2	8.0×10^{-10}	1.078687×10^{-2}	3.40×10^{-4}
	2.5×10^{-10}	7.6634×10^{-3}	4.0×10^{-4}
	1.5×10^{-10}	5.4517×10^{-3}	5.0×10^{-4}
J_3	4.1×10^{-11}	1.078275×10^{-2}	3.40×10^{-4}
	4.1×10^{-11}	7.61×10^{-3}	5.0×10^{-4}
	5.0×10^{-12}	5.286×10^{-3}	4.5×10^{-4}

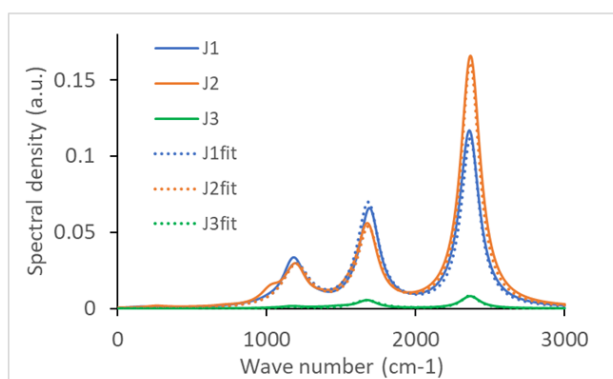


Figure 6: Spectral densities associated to the correlation functions for the three baths: J_1 tuning for D_1 , J_2 tuning for D_2 , and J_3 inter-state coupling. Solid lines: continuous functions from the LVC model obtained with the smoothing function, eq. (2); dotted lines: fit with the three Tannor-Meier Lorentzian functions.

5 Bath dynamics in HEOM

Some information about the bath dynamics during the relaxation can be extracted from the ADOs.⁴⁻⁷ For instance, the average value of each tuning collective mode, $\bar{X}_n = \bar{B}_n/D^{(n)}$ (with $n = 1, 2$), illustrates the trajectory toward the new equilibrium position. $\bar{B}_n(t)$ is obtained upon summing the corresponding diagonal elements of each ADO (referred to as with index j) of the first hierarchy level, $L = 1$, with a single-occupation number in the artificial modes of this bath n ,

$$\bar{B}_n(t) = -\sum_j \rho_{j,m}^{L=1}(t) \quad . \quad (4)$$

The normalisation factor is computed in the continuous case by

$$D^{(n)2} = \frac{2}{\pi} \int_0^\infty \omega J_n(\omega) d\omega \quad . \quad (5)$$

Figure 7 gives the average position of the collective mode of bath 1 or 2 when the initial state is in D_1 or D_2 , respectively. When the system is prepared in D_1 , one observes a fast motion far from the Franck-Condon region, followed by an oscillatory relaxation toward the equilibrium position of D_1 . Very little population reaches the D_2 state, so that the average remains quasi zero. A similar result would be obtained with a wavepacket having a vanishing norm in an excited state. When the preparation is in state D_2 , the transfer is ultrafast and the relaxation is overdamped and directly reaches the same equilibrium position in D_1 . Again, the norm of the remaining wavepacket in D_2 is negligible.

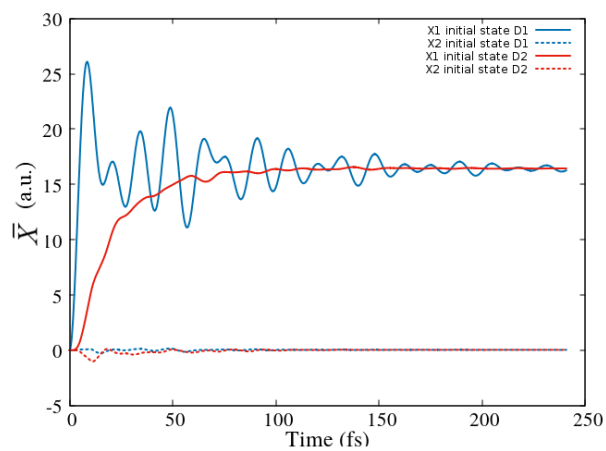


Figure 7: Time evolution of the expectation value for the collective mode \bar{X}_n (with $n = 1, 2$) for bath 1 (full lines) and 2 (dashed lines) when the initial state is D_1 or D_2 (blue and red, respectively).

6 Nonlinear spectroscopy

6.1 Additional cuts and slices through the ESE and TA spectrograms

The energy-resolved cuts through the ESE spectrograms for the 2L model presented in fig.8 of the main text are given in fig. 8 here. The corresponding cuts for the full 3L model are shown in fig. 9 in the main text. The spectra are less structured but the general behavior is the same, passing indeed from the absorption profile toward the emissive one.

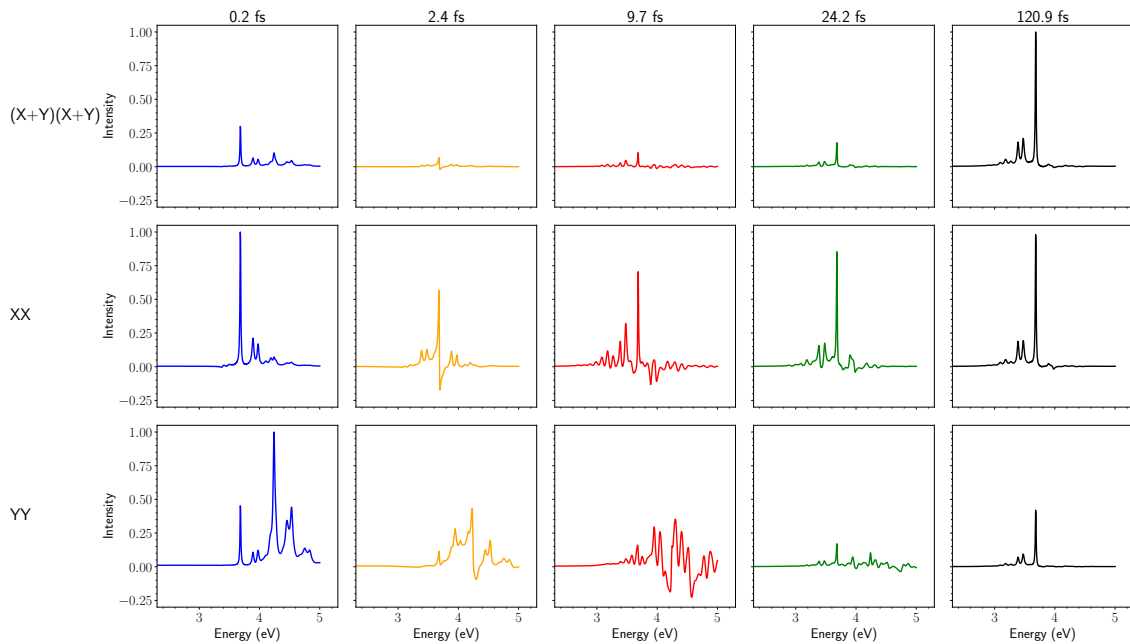


Figure 8: Energy-resolved cuts through the time-and-frequency-resolved ESE spectrograms for different pump-probe delays obtained in the full 2L model. The polarizations are along $(e_x + e_y)/\sqrt{2}$ (top), e_x (middle), and e_y (bottom). The spectra are normalized with the maximum intensity among spectra along the same line (with the same polarization).

In fig. 9 and fig. 10 here, we compare the evolution of the TA spectrum in the 2L and 3L models, respectively. Since the initial ESE spectrum is similar to the GSB one, the TA spectrum evolves from nearly twice the GSB spectrum, *i.e.*, twice the absorption spectrum, toward the sum of the absorption and the emission spectra. The 3L model, also discussed in the maint text, accounts for the additional effect of the low frequencies at room temperature but shows similar trends.

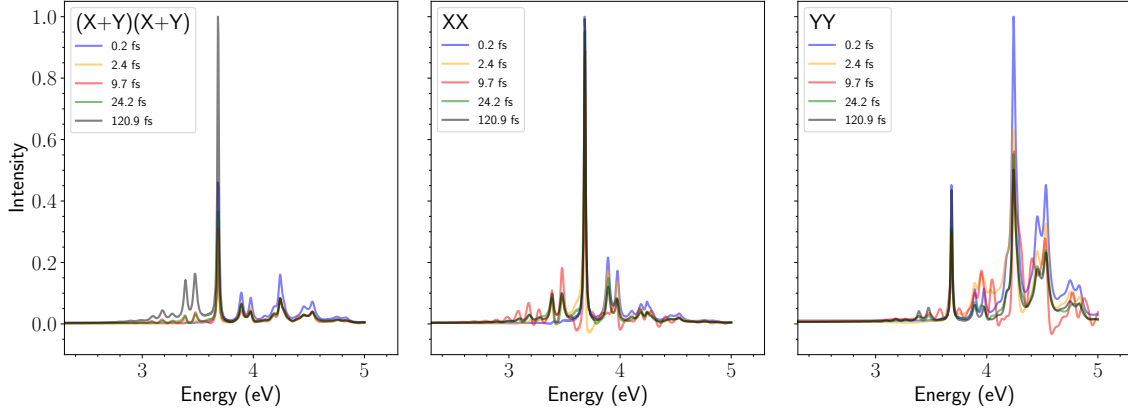


Figure 9: Energy-resolved cuts through the time-and-frequency-resolved TA spectrograms for different pump-probe delays obtained in the full 2L model. The polarizations are along $(e_x + e_y)/\sqrt{2}$ (left panel), e_x (center panel), and e_y (right panel). The spectra are normalized with the maximum intensity among spectra of the same panel (with the same polarization).

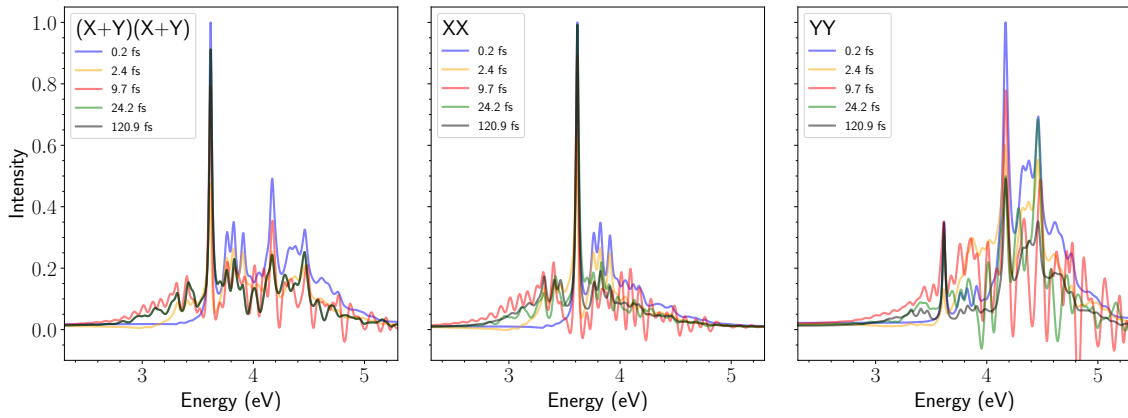


Figure 10: Energy-resolved cuts through the time-and-frequency-resolved TA spectrograms for different pump-probe delays obtained with the full 3L model. The polarizations are along $(e_x + e_y)/\sqrt{2}$ (left panel), e_x (center panel), and e_y (right panel). The spectra are normalized with the maximum intensity among spectra of the same panel (with the same polarization).

6.2 ESE signals in the uncoupled case

Figure 11 gives the ESE spectrograms obtained for the 2L model with polarizations XX and YY in the case where the coupling bath is discarded so that there is no inter-state coupling. This corresponds to a pure dephasing case where the populations remain constant but the initial electronic coherence is destroyed by the tuning baths.

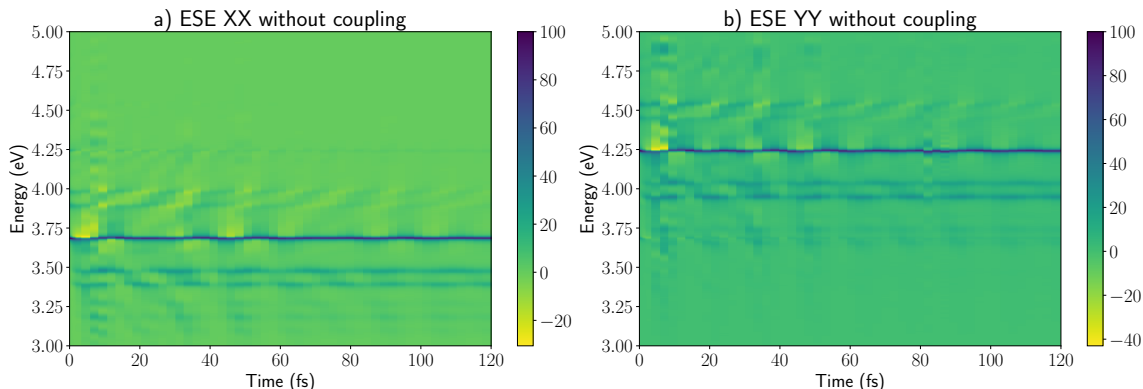


Figure 11: Time-and-frequency resolved ESE spectrograms when setting the inter-state coupling to zero, for the approximate 2L model with only the two high-frequency peaks in the spectral densities of fig. 6. The pump and probe are delta-like laser pulses. The polarizations are along e_x (left panel) or e_y (right panel).

The time-resolved horizontal slices through the ESE spectrograms are shown in fig. 12. They are selected at two different frequencies corresponding to distinct maxima in the absorption spectrum. The integrated ESE signals with and without the inter-state coupling are compared in fig. 13 with or without normalization.

Finally, in fig. 14, we illustrate that the Fano profile observed in the ESE spectra for a delay of about 2.5 fs is not due to the nonadiabatic transitions since it remains when the inter-state coupling is cancelled.

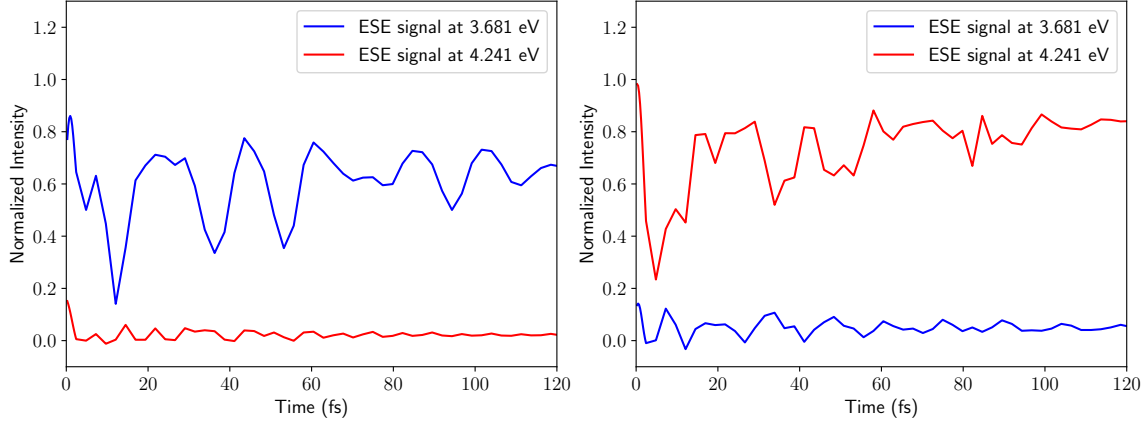


Figure 12: Time-resolved slices through the ESE spectrograms when setting the inter-state coupling to zero (fig. 11) at two different frequencies corresponding to distinct maxima in the absorption spectrum. The polarizations are along e_x (left panel) or e_y (right panel).

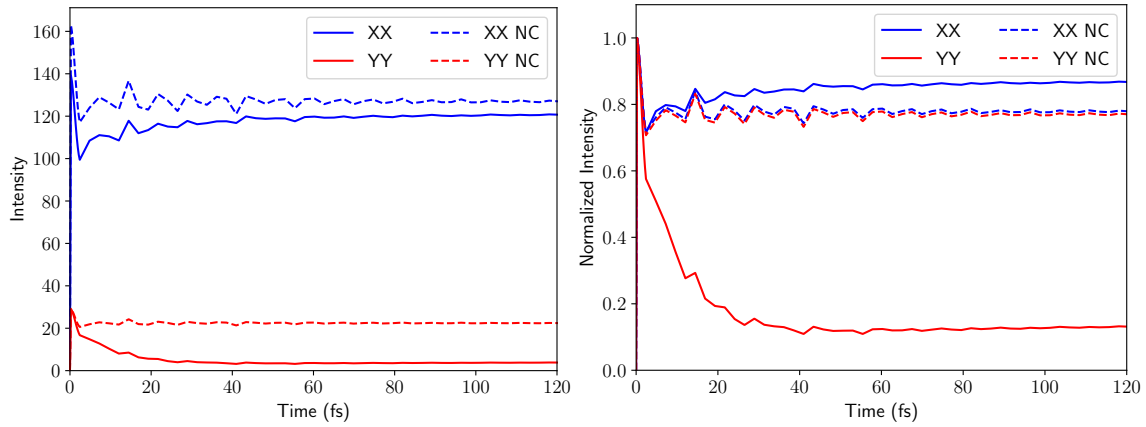


Figure 13: Integrated ESE signal, $S^{\text{ESE}}(t)$, for pump-probe polarizations e_x or e_y with and without inter-state coupling (NC: no coupling bath), as plain and dashed lines, respectively. The right panel corresponds to normalized signals for each polarization.

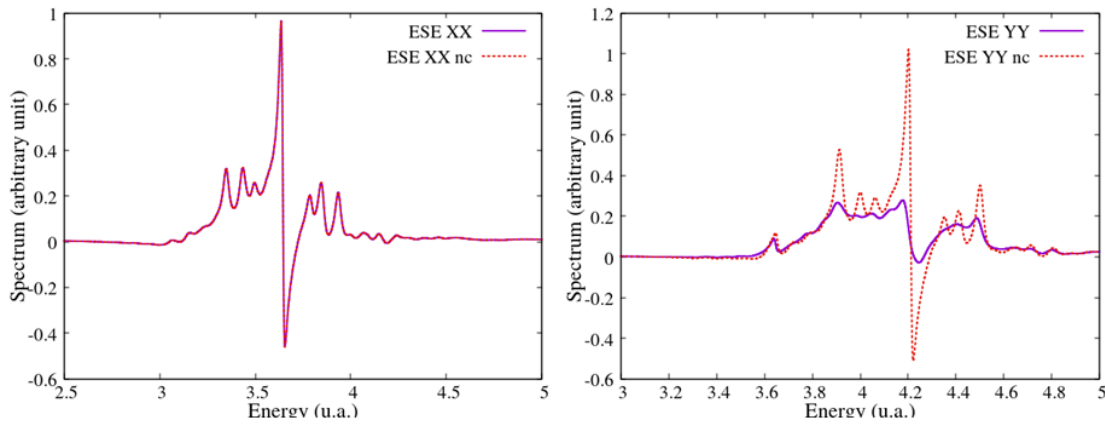


Figure 14: ESE spectra with and without inter-state coupling (nc: no coupling) for the 3L model at 2.4 fs. The polarizations are along e_x (left panel) or e_y (right panel).

References

- (1) Galiana, J.; Lasorne, B. Excitation energy transfer and vibronic relaxation through light-harvesting dendrimer building blocks: A nonadiabatic perspective. *The Journal of Chemical Physics* **2024**, *160*, 104104.
- (2) Meier, C.; Tannor, D. J. Non-Markovian Evolution of the Density Operator in the Presence of Strong Laser Fields. *J. Chem. Phys.* **1999**, *111*, 3365–3376.
- (3) Pomyalov, A.; Meier, C.; Tannor, D. J. The Importance of Initial Correlations in Rate Dynamics: A Consistent Non-Markovian Master Equation Approach. *Chem. Phys.* **2010**, *370*, 98–108.
- (4) Zhu, L.; Liu, H.; Xie, W.; Shi, Q. Explicit system-bath correlation calculated using the hierarchical equations of motion method. *The Journal of Chemical Physics* **2012**, *137*, 194106.
- (5) Liu, H.; Zhu, L.; Bai, S.; Shi, Q. Reduced quantum dynamics with arbitrary bath spectral densities: Hierarchical equations of motion based on several different bath decomposition schemes. *The Journal of Chemical Physics* **2014**, *140*, 134106.
- (6) Mangaud, E.; Meier, C.; Desouter-Lecomte, M. Analysis of the non-Markovianity for electron transfer reactions in an oligothiophene-fullerene heterojunction. *Chemical Physics* **2017**, *494*, 90–102.
- (7) Mangaud, E.; Lasorne, B.; Atabek, O.; Desouter-Lecomte, M. Statistical distributions of the tuning and coupling collective modes at a conical intersection using the hierarchical equations of motion. *The Journal of Chemical Physics* **2019**, *151*, 244102.